1   Title: Tumor cell phenotype and heterogeneity differences in IDH1 mutant vs wild-type gliomas

2   Short title: Tumor cell phenotype and heterogeneity differences in IDH1 mutant vs wild-type gliomas

3   Michael E. Berens[1,¶], Anup Sood[3,¶], Jill S. Barnholtz-Sloan[2,¶], John F. Graf[3], Sanghee Cho[3], Seungchan
4   Kim[4], Jeffrey Kiefer[1,#a], Sara A. Byron[1], Rebecca F. Halperin[1], Sara Nasser[1], Jonathan Adkins[1], Lori
5   Cuyugan[1], Karen Devine[2], Quinn Ostrom[2], Marta Couce[2], Leo Wolansky[2,#b], Elizabeth McDonough[3],
6   Shannon Schyberg[3], Sean Dinn[3], Andrew E. Sloan[7], Michael Prados[5], Joanna J. Phillips[5], Sarah J. Nelson[6],
7   Winnie S. Liang[1], Mirabela Rusu[3,#c], Maria I. Zavodszky[3,#d], Fiona Ginty[3]

8

9   [1]Brain Tumor Unit, Cancer and Cell Biology Division, Translational Genomics Research Institute, Phoenix,

10   Arizona, United States of America

11   [2]Department of Population and Quantitative Health Sciences and Case Comprehensive Cancer Center,

12   Case Western Reserve University School of Medicine, Cleveland, Ohio, United States of America

13   [3]GE Research Center, Niskayuna, New York, United States of America

14   [4]Department of Electrical and Computer Engineering, Roy G. Perry College of Engineering, Prairie View

15   A&M University, Prairie View, Texas, United States of America

16   [5]Department of Neurological Surgery, Helen Diller Cancer Center, University of California San Francisco,

17   San Francisco, California, United States of America

18   [6]Department of Radiology and Biomedical Imaging, University of California, San Francisco, California,

19   United States of America

20   [7]Department of Neurosurgery, University Hospitals-Seidman Cancer Center, Cleveland, Ohio, United

21   States of America

22   [#a]Current Address: Systems Oncology, Scottsdale, Arizona, United States of America

23   #bCurrent Address: Department of Diagnostic Imaging and Therapeutics, UConn Health, Connecticut,

24   United States of America

25   #cCurrent Address: Stanford University, Department of Radiology, Stanford, California, United States of

26   America

27   #dCurrent Address: Biogen, Cambridge, Massachusetts, United States of America

28

29   *Corresponding author

30   Email: mberens@tgen.org

31   ¶ Joint first authors

32

Abstract

34   Glioma is recognized to be a highly heterogeneous CNS malignancy, whose diverse cellular composition

35   and cellular interactions have not been well characterized. To gain new clinical- and biological-insights

36   into the genetically-bifurcated IDH1 mutant (mt) vs wildtype (wt) forms of glioma, we integrated

37   multiplexed immunofluorescence single cell data for 43 protein markers across cancer hallmarks, in

38   addition to cell spatial metrics, genomic sequencing and magnetic resonance imaging (MRI) quantitative

39   features. Molecular and spatial heterogeneity scores for angiogenesis and cell invasion differ between

40   IDHmt and wt gliomas irrespective of prior treatment and tumor grade; these differences also persisted

41   in the MR imaging features of peritumoral edema and contrast enhancement volumes. Longer overall

2

42   survival for IDH1mt glioma patients may reflect generalized altered cellular, molecular, spatial

43   heterogeneity which manifest in discernable radiological manifestations.

44

45   **Introduction**

46   Gliomas represent the most common type of malignant brain tumor, comprising 81% of malignant brain

47   and central nervous system (CNS) tumors and 27% of all brain and CNS tumors in the United States(1).

48   While gliomas are relatively rare in the general population with an average annual age-adjusted

49   incidence of 6.2 per 100,000, these primary brain tumors contribute significant morbidity and mortality,

50   with glioblastoma carrying a 5-year survival rate of less than 6%(1).

51

52   The landscape of our knowledge about molecular features required for accurate diagnosis and prognosis

53   for glioma patients has advanced greatly in the last decade (2-5). Molecular subclassification highlights

54   different genetic underpinnings of glioblastoma (6), which offer some prognostic insight (7), likely

55   attributable, in part, to gene expression patterns influencing vulnerability to radiation (8). The World

56   Health Organization (WHO) classifies gliomas into defined categories based upon histologic and

57   molecular features and are assigned into four grades of increasing aggressiveness. Additionally, the

58   methylation status of O6-methylguanine-DNA methyltransferase (MGMT) has been implicated as a

59   useful biomarker for conferring tumor resistance to alkylating chemotherapies; methylation of the

60   MGMT promoter leads to transcriptional silencing of MGMT, which is associated with loss of MGMT

61   expression and increased response to alkylating chemotherapies such as temozolomide (TMZ) (9).

62   Analysis of DNA methylation from gliomas identified a DNA methylation-based phenotype, G-CIMP,

63   which is characterized by global hypermethylation of CpG islands and is predictive of increased survival;

64   this G-CIMP phenotype is associated with isocitrate dehydrogenase (IDH) mutation status (3, 4, 10).

65

66   *IDH* wild type (wt) in histologically defined low-grade gliomas is associated with poor clinical prognosis

67   that more resembles glioblastoma multiforme (GBM), which generally lack *IDH* mutation (IDHmt) (3, 11).

68   Conversely, *IDH* mutations are observed in the majority of lower-grade gliomas and are associated with

69   better clinical outcomes. In low-grade gliomas with *IDH* mutations, 1p/19q codeletion is further

70   associated with oligodendrogliomas and better chemotherapeutic response (12). The validation of some

71   of these molecular biomarkers for diagnosis and prognosis has prompted WHO to include molecular

72   subclasses into their latest classification schema for CNS tumors, including addition of MGMT

73   methylation and IDH-mutant/IDH-wildtype classifications for glioblastoma, as well as IDH-mutant and

74   1p/19q-codeleted classifications for oligodendrogliomas and anaplastic oligodendrogliomas (13).

75   Intratumoral heterogeneity, even across molecular subtypes, is now also appreciated as a characteristic

76   of glioma and glioblastoma (14) and has been shown to occur temporally (15), spatially (16) (17), for

77   oncogenic drivers (18), and through the stem cell lineage (19). Heterogeneity features have been

78   identified by radiologic imaging with quantitative features, including distinguishing between IDH1mt vs

79   wt gliomas(20) . While these and other studies have interrogated glioma heterogeneity using bulk

80   transcriptomics and single cell sequencing, medical imaging has also provided valuable heterogeneity

81   insights (albeit limited by resolution e.g. 1 voxel, the volumetric unit, in a 1.5 T MRI image contains

82   approx. 1-2 million cells). There have been no investigations to date of cell-level spatial heterogeneity in

83   protein expression or cell types and how they relate to the radiological appearance of these tumors on

84   MRI. Understanding malignant progression in IDH1 mt and wt patients at multiple scales and in a spatial

85   context is pivotal to delineating biological events underlying glial tumors and may facilitate tailored

86   treatment approaches as well as reveal new therapeutic targets. Moreover, this multi-scale

87   characterization may facilitate the identification of quantitative metrics derived from non-invasive

88   imaging, i.e. MRI, which correlate with or predict molecular and cellular phenotypes. Such metrics may

4

89   be evaluated for new patients prior to biopsy or surgery and might inform about the presence of certain

90   cellular characteristics that may affect treatment response or outcome.

91

92   To discern multimodal differences in relation to IDHmt status, we conducted a multiscale interrogative

93   workflow which combines multiplexed immunofluorescence and single cell spatial analysis of fixed

94   glioma tissue, bulk genomic tumor sequencing, MR imaging quantitative features of the whole tumor

95   and subregions, and patient outcomes. Multiscale datasets were assembled from treatment-naïve cases

96   of grade 2, 3, and 4 astrocytoma/oligodendroglioma (n=20, referred as treatment-naïve glioma) as well

97   as from recurrent (previously-treated) grade 4 astrocytoma (glioblastoma) (n=16, referred as recurrent

98   GBM). Tumor tissue punches from diagnostic paraffin blocks were assembled in duplicate (glioma) or

99   triplicate (recurrent GBM) into tissue microarrays for multiplex immunofluorescence staining (21) using

100   43 markers to identify cell types and functional states corresponding to cancer hallmarks (22). Exome

101   sequencing data was processed for mutations, copy number aberrations, as well as insertions and

102   deletions. Deconvolution of gene expression data from bulk tumor specimens afforded comparisons of

103   protein levels and transcript levels across cognate specimens. An expert neuroradiologist (LW) outlined

104   on MRI of the treatment naïve glioma, and of recurrent GBM (SJN), while advanced deep learning

105   methods were utilized to delineate necrotic and enhancing cores, as well as peri-tumororal edema.

106   Morphologic features assessed the volumes of the different regions and their ratios, while simple

107   features, T1 weighted post contrast (T1 Post), Apparent Diffusion Coefficient (ADC), and Fluid

108   Attenuated Inversion Recovery (FLAIR), were extracted from different MRI protocols.

109   Various MRI-focused studies (23-26) have investigated the ability of imaging features to predict IDH1

110   mutational status. Studies focused on assessing the tumor volume, contrast enhancement status (27),

111   Visually AcceSAble Rembrandt Images (Vasari) feature set (28, 29), radiomics features (30) or features

112   that were derived via convolutional neural networks (31), among others and used these to train

5

113   predictive models of IDH1 mutational status. These studies showed great ability to predict IDH1

114   mutational status with accuracies as high as 89.1% and area under the receiver operator curves (AUC) of

115   0.95. Other radiogenomic studies have revealed the correlation of IDH1 mutational status with hypoxia

116   induced angiogenesis and identified that the relative cerebral blood volume (rCBV) MRI was able to

117   predict IDH1 mutations status with an 88% accuracy (32). Unlike the latter studies that predict IDH1

118   mutatinal status, we seek to reveal correlations between MRI derived quantitative features, cellular

119   composition and spatial cellular heterogeneity to understand the mechanism of disease progression in

120   relation to IDH1 mutational status. Such knowledge could enable creation of predictive models on MRI

121   of disease progression or treatment response without the need for an invasive biopsy.

122   We show lower cell-level protein expression in IDH1mt vs wt cases. Further, IDH1mt gliomas,

123   irrespective of grade, showed greater spatial heterogeneity but lower molecular heterogeneity of

124   biomarkers associated with angiogenesis (VEGR2, CD31, SMA, S100A4) and invasion (n-cadherin, cofilin,

125   collagen IV, GFAP and vimentin). Similarly, cell classes derived from deconvolution of bulk gene

126   expression data showed the cell class with high expression of most hallmark genes, particularly those

127   belonging to enabling replicative immortality, evading growth suppressors and inducing angiogenesis,

128   were significantly under represented (<10%) in the IDHmt tumors. IDH mutation was co-expressed with

129   ATRX mutations and was mutually exclusive of EGFR and PTEN mutations consistent with known tumor

130   biology. Longer overall survival following diagnosis for IDH1mt glioma patients may reflect generalized

131   altered cellular, molecular and spatial heterogeneity, which is also reflected in the MR images as lower

132   enhancement and higher edema.

133   # Materials and Methods

134   ## Patient cohorts

135   Cohorts of 20 treatment-naïve gliomas (grades 2, 3, and 4 from the Ohio Brain Tumor Study) and 16

136   post-treatment recurrent glioblastoma (grade 4 from University of California San Francisco(33)) were

137   retrieved based on appropriate patient consent, suitable MR images, FFPE tissue availability, and

138   specimens suitable for next-generation sequencing (**Table 1 for patient summary and S-Tables S-1 and**

139   **S-2 for additional details**).

140   **Table 1: Summary of patient characteristics of glioma and recurrent GBM cohorts**

141

142

143

144

145

146

147

148

149

150

151

152

153

154

155

156

157

158

Cohort	Treatment naïve primary glioma patients	Recurrent/Refractory GBM patients
Patient number	20	16
Median (range) age at diagnosis (years)	57 (26-77)	51 (29-66)
Gender		
Male	12	12
Female	8	4
Ethnicity		
Caucasian	18	15
Hispanic, Asian, African American	0,1,1	1,0,0
Histologic grade		
II	5	-
III	7	-
IV	8	16
IDH1/2 mutation status		
Mutant (IDH1 R132H)	8	3
Wildtype	12	13
1p19q codeletion		
Codeletion	4	-
Non-codeletion	11	-
Not available	5	-
Median (range) survival (days)		
Grade II	1120 (420-2326)	-
Grade III	487 (370-2964)	-
Grade IV (GBM)	438 (222-541)	1031 (396-3771)

159

160

Workflow for multi-modal data generation and integration

162   Using the methods provided below, three parallel analytical interrogations of the treatment-naive

163   glioma and recurrent cases were pursued: multiparametric MRI; multiplexed immunofluorescence tissue

164   imaging; and RNA and DNA sequencing. **Fig. 1** depicts the overall workflow for this multi-modal data

165   generation, including multiple analytical approaches to cluster and differentiate clinically variable

166   phenotypes. Given the two cohorts of different clinical characteristics and the multi-modal nature of

167   the data, our analysis was performed stratified by cohort, yet we aimed at identifying associations that

168   are consistent across the two cohorts.

169   **Fig. 1. Overall workflow for generating multi-scale, multiparametric data, extraction of**

170   **various features and/or conversion to higher scales and multiple analysis approaches**

171   **to differentiate clinically variable phenotypes.** Multi-parametric MRIs (Panels A & B)

172   were segmented for ROIs and various image features to characterize tumor and

173   subregions (necrosis, enhancing and edema) within the tumor. Multiplexed

174   immunofluorescence tissue analysis (Cell DIVE) (Panel C) provides (left-to-right) a virtual

175   H&E (vH&E), which is a pseudo-colored DAPI and AF image, and corresponding overlays

176   of 46 markers (examples shown are for proliferation and angiogenesis markers). Single

177   cell data were generated for every multiplexed marker and intensity binned into 3 tiers

178   (low, medium or high) for each cell. Cell level biomarker data was integrated with

179   known biological pathways knowledge base and used to compute molecular states of

180   individual cells. For visualization purposes, the molecular state of a cell is overlaid on the

181   vH&E image (Panel D). Genomics data (Panel E & F), including IDH1 mutation status,

182   were summarized into pathways, cancer hallmarks, and enrichments for each tumor.

183   Cell-level and MRI feature data were clustered across all glioma patients and by IDH 1

184   status (Panel G); finally, molecular and spatial heterogeneity were analyzed relative to

185   IDH1 mutation status or tumor grade (Panel H).

186

187   Multiplexed immunofluorescence imaging of disease and cellular

188   biomarkers

189   Using the original diagnostic FFPE tissue blocks of each case studied, dual (treatment-naïve glioma) or

190   triplicate punches (recurrent GBM) were selected for tissue microarray (TMA) construction and

191   subsequent multiplex immunofluorescence staining and imaging (MxIF). Two replicate slides were used

9

192   for the treatment-naïve glioma TMAs and 3 replicate slides were used for the recurrent GBM TMAs.

193   Control cores (2 per cancer type) were included on all slides for glioma, prostate, melanoma, lung,

194   breast cancer to verify antibody performance. Briefly, the Cell DIVE™ platform (GEHC), which allows in

195   situ probing of up to 60 biomarkers in a single 5um FFPE TMA tissue section, followed by image

196   processing, registration and single cell analysis, was used (21) (**S1 A-C Fig.**). After a two-step antigen

197   retrieval step, the sample underwent repeated cycles of staining, imaging and dye signal quenching **(S1-**

198   **A Fig.)** for a total of 43 biomarkers **(S3 Table),** representing members of different cancer hallmarks, cell

199   lineage and cell segmentation(22). Markers of iron metabolism were also included as ferroptosis is an

200   emerging field of study with mechanistic ties to glioma cell resistance to therapy (34-36). Antibody

201   clones, staining concentrations and staining sequence are provided in **S3 Table**. The detailed process for

202   antibody validation (testing, conjugation and verification) is described in **S2 Fig.** and described in S

203   information of Gerdes et al (21). Prior to storage, images are automatically processed for illumination

204   correction, registration from multiple rounds using the DAPI image acquired in each round and

205   background (tissue autofluorescence, AF) removal by subtracting the image of tissue acquired prior to

206   staining from the image after staining **(S1-B Fig.)**.

207

Image quality checks, processing and cell segmentation

208

209   Staining quality of all multiplexed images was assessed by visual assessment of staining patterns of

210   individual markers in all samples and compared to controls and/or expected patterns. Since replicate

211   slides were also available, staining intensities were compared across slides. Staining profiles between

212   the treatment-naïve glioma and recurrent GBM cohorts were also compared. Markers that failed or had

213   non-specific staining or very low or negative expression across the whole cohort were excluded from

214   analysis **(S3 A-C Fig.)**. The single cell analysis workflow consists of segmentation and quantification steps

215   **(S1-C Fig.)**. First, image background was suppressed using top-hat filtering followed by multi-level image

216   thresholding. Second, nuclei were segmented using a wavelet-based algorithm that uses both nuclei

217   intensity and shape (blobness) information (37). Nuclear segmentation was followed by whole-cell

218   segmentation, where synthetic cell boundary was extracted by applying Voronoi tessellation using the

219   nuclei as seeds. To avoid producing very large cells from isolated nuclei, a constraint on the maximum

220   distance between the nucleus and the corresponding cell boundary was applied. Segmented images

221   were visually assessed for segmentation quality and compared with images of DAPI staining and virtual

222   H&E (generated from pseudo-color overlays of DAPI and tissue AF). A single image (1 of 40 (treatment-

223   naïve glioma) failed segmentation due to poor tissue quality. Five images (of 46 total images) from

224   recurrent GBM patients were removed from analysis as these cores contained few (<10%) tumor cells or

225   were cauterized.

226

227   The cell segmentation steps were followed by quantification of biomarker intensities in each cell, as well

228   as cell features and morphological properties. The entire set of cell-based measurements, including their

229   IDs and spatial coordinates, are saved as .csv files for statistical analysis in R. For each tissue core, image

230   registration quality was determined based on DAPI correlation with baseline round. Further, using

231   correlation of DAPI signal at cell level from each staining/imaging round, a quality score was generated

232   for every cell in each image, which ranges from 0-1 (0 being no registration, up to 1 for perfect

233   registration). Only cells with quality score above 0.85 were included in the analysis. Scores below 0.5 are

234   generally due to tissue shifting/movement and loss. Excellent correlations **(S4 Fig.)** in number of cells

235   per replicate slide were found for the replicate treatment-naïve glioma TMAs and 2 of the recurrent

236   GBM slides (>0.98). Slightly greater cell heterogeneity was found for one of the recurrent GBM slides but

237   slide to slide correlation was still high (0.74).

238

11

Identification of cell clusters and biomarker co-expression

239

240   After exclusion of segmentation markers and single-cell MxIF markers which failed QC or staining criteria

241   as described above and shown in **S3 Fig.**, unsupervised cell clustering was performed with all the

242   remaining markers (n=24) using data from reported subcellular staining location (compartments used,

243   shown in **S3-A Fig.**). In total, 85,767 cells (from 20 treatment-naïve glioma cases) and 56,304 cells (from

244   recurrent GBM cases) remained for analysis. Separately, clustering was also conducted with smaller

245   subsets of markers representing individual hallmarks (angiogenesis, proliferation, invasion and motility).

246   Log2-transformed median cell intensity for each marker was used for K-means clustering. After trimming

247   to reduce the impact of extreme outliers at both 2.5% tails, and since the distribution of marker

248   intensity/expression values varies significantly within and between marker type, median cell biomarker

249   values were standardized by the overall marker mean and standard deviation.

250

251   Cells were clustered into K groups based on the multi-dimensional marker space (equivalent to number

252   of markers used for clustering). The *kmeans* function provided by *stat* package of *R* (v. 3.4.1) was used

253   with K (= 2 to 15). We used 10 random starts (nstart = 10) to address K-means clustering algorithm's

254   sensitivity to initial seeds. We also used multiple metrics to determine the best number of clusters for

255   the data such as Silhouette width, Calinsky criterion, Sum of squares of errors, and consensus clustering

256   metrics. For consensus clustering (R ConsensusClusterPlus package), a subset of 5,000 randomly

257   selected cells (due to computational constraints) were used. Consensus clustering iterates the clustering

258   algorithm and examines if each pair of samples consistently clusters together or not. K-means clustering

259   with Euclidean distance as metric was used for 1,000 iterations with 80% resampling. The cumulative

260   distribution function (CDF) plot and the heatmap from consensus clustering were evaluated to guide us

261   to determine the best number of clusters, aided by other metrics mentioned above. For a given K, each

262   cell was assigned to one of the K clusters, and each tumor sample represented according to the

263   proportion of cells belonging to one of the K clusters. For the purposes of data visualization and

264   interpretation, data was aligned by cluster, IDH1 mutation and patient ID. Biomarker intensities were

265   grouped by cancer hallmarks (invasion; energy metabolism; angiogenesis; stem cells; immune response;

266   proliferation; resisting cell death; DNA damage) and iron metabolism.

Exome and RNA Sequencing

268   Tumor and normal whole-exome sequencing and tumor RNA-sequencing data from the 20 treatment-

269   naïve gliomas was studied; data was either produced from fresh-frozen tissue (n=16, 8 of which had

270   been sequenced in The Cancer Genome Atlas) or from FFPE tissue (n=4) **(S1 Table).** Twelve of these

271   were newly accessed for de novo analysis, and the remaining data was already available. Pathology

272   estimates suggested those 12 samples all had greater than 70% tumor cell density and less than 50%

273   necrosis. Data from sixteen post-treatment recurrent fresh-frozen glioblastoma tumors previously

274   sequenced as part of a clinical trial (33) (data available in the database of Genotypes and Phenotypes

275   (dbGaP) under accession number phs001460.v1.p1) was also included **(S2 Table)**. All 16 of these tumors

276   had whole-exome sequencing data, and fourteen had cognate RNA-sequencing data available.

277

278   Constitutional DNA from PBMCs was available for all 36 samples. For the eight fresh frozen glioma

279   samples, Qiagen AllPrep DNA/RNA Mini Kit (cat#80204) was used to isolate DNA and RNA; for the four

280   FFPE treatment-naïve glioma samples, Qiagen AllPrep DNA/RNA FFPE Kit (cat# 80234) was used. Exome

281   libraries were constructed from 200ng of DNA (DIN=3-5 for FFPE samples, DIN >8 for blood and fresh

282   frozen samples) using KAPA Biosystems' Hyper Prep Kit (cat#KK8504) and Agilent's SureSelectXT V5

283   baits, containing custom content, following the manufacturer's protocols. Custom bait content included

284   copy number probes distributed across the entire genome, along with additional probes targeting tumor

285   suppressor genes and genes involved in common cancer translocations to enable structural analysis. For

13

286   high quality RNA (RIN>6.0, DV200>90%), RNA libraries were constructed using Illumina's TruSeq RNA

287   Library Preparation Kit V2 (cat#RS-122-2001) with 500ng inputs. For remaining RNAs (RIN<6,

288   DV200>30%), libraries were prepared using Illumina's TruSeq RNA Access Library Prep Kit (cat#RS-301-

289   2001) with either 40ng or 100ng inputs following the manufacturer's protocol and sample quality/input

290   recommendations. Libraries were equimolarly pooled, quantitated, and sequenced by synthesis on the

291   Illumina HiSeq 4000 for paired 82bp reads. FASTQ were aligned using bwa-mem (version 0.7.8) to the

292   reference genome from 1000 Genomes project build hs37d5 with decoy contigs [b37d5] and Ensembl

293   v74 for annotations. Somatic variants were called using lumosVar2 (38). For this study, a tumor-normal

294   mode was used which the sample fraction of clonal variant groups is set to zero in the constitutional

295   sample.

296 Deconvolution of samples into cell classes from RNAseq data of bulk

297 samples

298   Multiple cell classes, characterized by different dominant biological processes, can be discerned by

299   computational deconvolution of bulk gene expression data obtained from complex samples (39, 40).

300   This approach is a practical alternative when available samples are not suitable or available for single-

301   cell sequencing (scRNAseq). Deconvolution assumes that the analyzed sample is composed of a certain

302   number of cell types or different cell states, called *classes*. These classes do not necessarily fall into

303   mutually-exclusive cell types. Instead, they represent quantifiable components of the analyzed samples

304   that exhibit distinct gene- or pathway-attributable behaviors. We employed the previously published

305   CellDistinguisher algorithm to identify sets of genes that are expressed predominantly in one class

306   relative to the others (41). As demonstrated in the Results, gene sets of ~50 genes led to robust

307   assignments of cells into three classes. These distinguisher gene sets were then used to derive class

308   signatures and compute sample compositions (fractions of cell types or classes in each sample) using the

309   SSKL algorithm from the CellMix package (42). To validate and support our findings with the multiplexed

310   single cell data, we also explored how well cell type assignments based on gene expression data

311   compared to those based on protein expression measured by MxIF.

312

313   Calculation of molecular and spatial cell heterogeneity metrics

314   Molecular and spatial heterogeneity metrics were computed for the MxIF spatially resolved cell data

315   using a previously published heterogeneity analysis algorithm (MOHA) (43). As described in more detail

316   below, this technique computes the molecular "state" of each cell in a tissue section based on the

317   fluorescence intensity of proteins within a given pathway, gene set or cancer hallmark (22). Spatial

318   "states" is a summated score which depicts the degree to which adjacent cells are of the same

319   molecular state. The MOHA algorithm computes heterogeneity (or similarity or divergent states)

320   metrics based on the distributions of these molecular and spatially defined states.

321

322   The molecular state of a given cell was defined as an ordered set of the values for each individual

323   marker. A complete list of the cancer hallmark gene sets and the markers that were assigned to them is

324   shown in **S3 Table**. The state of each marker was quantized into an ordinal value representing either a

325   high, medium or low state, using the 33rd and 67th quantiles as the thresholds. The specific ordering of

326   the markers in a given gene set (i.e. concatenation sequence) is arbitrary but was maintained

327   consistently throughout the analysis. This process of computing the molecular state was repeated for

328   each cancer hallmark marker set and for each cell. Next molecular heterogeneity metrics were

329   computed as a normalized Shannon's entropy of molecular states:

330

331
$$Molecular\ Heterogeneity = \frac{-\sum_{i=1}^{Nm} Pm_i \ \ln(Pm_i)}{\ln(Nm)}$$

332   The Pm_i is the fraction of cells in molecular state i, and Nm is the number of possible molecular states in

333   the system. The number of possible states for a gene set was defined as three raised to the power of the

334   number of markers assigned to the gene set (e.g. 3^number of markers). The molecular heterogeneity

335   metric value can range from zero to unity (i.e. maximum heterogeneity). For each patient tissue sample,

336   a molecular heterogeneity metric was computed for each cancer hallmark.

337   Cell Spatial Heterogeneity is a summated score which depicts the degree to which adjacent cells are of

338   the same molecular state as that of an index cell, with each cell in the tissue section serving as an index

339   cell **(Example shown in S5 Fig.)**. Identifying neighboring cells is necessary for computing the spatial

340   heterogeneity metrics. Two cells were classified as neighbors if the Euclidean distance between the

341   centers of the two cells was less than 1.3 times the sum of their radii. The cell radii were computed from

342   the segmented cell area after approximating the cell as a circle. The spatial state metric was computed

343   by surveying the neighbors of each cell and counting only the number of neighbors in the same

344   molecular state. This number of neighbors represents the cell spatial state for each pathway or gene set.

345   Having no neighbors in the same molecular state is a valid cell spatial state. Therefore, the cell spatial

346   state can range from zero to the maximum number of neighbors a cell has. After going through every

347   cell and their neighbors, a frequency distribution was established for these cell spatial states. The cell

348   spatial heterogeneity was then computed as a normalized Shannon's entropy of spatial states:

349
$$Cell\ Spatial\ Heterogeneity = \frac{-\sum_{k=0}^{Z_{max}} Ps_k \ \ln(Ps_k)}{\ln(Z_{max}+1)}$$

16

350 where, Ps_k is the probability of state k, and Z_{max} is the maximum number of neighbors a cell can have as

351 measured in the tissue sample. For each patient tissue sample, a spatial heterogeneity metric was

352 computed for each cancer hallmark.

MRI imaging protocols and image feature extraction

353

354 The multi-parametric MRI (mpMRI) exams of the brain consisted of T2-weighted (T2), T1 weighted pre-

355 contrast (T1 Pre), T1 weighted post contrast (T1 Post), Apparent Diffusion Coefficient (ADC) derived

356 from diffusion-weighted imaging (DWI), and Fluid Attenuated Inversion Recovery (FLAIR) images. The

357 subjects with recurrent GBM were imaged using 3 Tesla GE scanners, while the treatment naïve subjects

358 were imaged at a different institution using 3 Tesla Siemens scanners. Although the acquisitions were

359 consistent in sequence types across institutions, parameters such as relaxation and echo times were

360 different, thus prompting separate image analysis for the two cohorts.

361

362 Tumor annotations on the MR images were manually outlined by an expert neuroradiologist to depict

363 the extent of the whole tumor, including peritumoral regions, relative to the FLAIR sequence. To the

364 extent possible, an equivalent normal region on the contra-lateral side of the brain was demarcated. A

365 deep learning approach was trained on the Brain Tumor Segmentation (BraTS) challenge data (44) and

366 was utilized to divide the whole tumor segmentation into enhancing core and necrotic core based on T1-

367 post contrast MRI. A U-net network was trained using the T1 Post contrast MRI to identify the extent of

368 the enhancing and necrotic cores on the BraTS data. The training code and trained model are available

369 (https://github.com/mirabelarusu/deep_learning_inference_browser). The trained model was

370 subsequently applied on the T1 post contrast MR images for the patients in our cohort to segment the

371 enhancing and necrotic cores. The peri-tumoral (edema) regions were obtained by subtracting the

372 enhancing and necrotic core from the whole tumor segmentation. Manual corrections and automatic

373   postprocessing were utilized when appropriate to improve the precision of the annotations or remove

374   minor disconnected regions. At the completion of these processing steps, an annotation of the whole

375   tumor, the peritumoral (edema) region, enhancing core, and necrosis were obtained for each subject

376   relative to the FLAIR protocol.

377   Pre-processing steps were applied on the mpMRI prior to feature extraction, including spatial

378   registration to align the FLAIR protocol relative to the others, in order to project the region annotations

379   on the rest of the protocols. Intensity normalization was applied in the entire organ by using the normal

380   regions as reference. Specifically, the intensities were normalized such that the average intensity in the

381   normal region had a value of 1. To perform this normalization, we divided the intensity of each voxel by

382   the average of intensities within the normal region.

383   Image derived quantitative features were evaluated for each subject. Due to the limited number of

384   subjects in our study, the large number of protocols (n=5) available for each subject and the multiple

385   subregions available for each tumor (n=4), we chose to consider only three protocols (T1-post, FLAIR

386   and ADC) and three tumor subregions (the whole tumor, the peritumoral edema and enhancing core).

387   We represented the tumor subregions by two image-derived quantitative features (mean and standard

388   deviation), resulting in 18 image-derived features per subject. Also, for each subject, we included three

389   morphologic features (the volume of the enhancing core, the volume of the entire tumor and their ratio

390   – which we refer to as the normalized enhancing core volume).

391   **Multimodality data integration and clustering**

392   Finally, we investigated the associations between imaging quantitative features and other variables

393   including cell cluster data, clinical parameters and cancer hallmarks based on cell protein expression,

394   RNA and DNA. Due to the different source and scales of the multimodal data (clinical, MxIF, genomic,

395   MRI), we discretized the most relevant features into "low", "medium" and "high" groups, based on the

18

396   data ranges across the individual cohorts. Features were considered to be relevant for the multimodal

397   association analysis either because there were clinically utilized for decision making, e.g. IDH1 mutation

398   status, age, and grade, or because they showed consistent trends across both treatment naïve subjects

399   as well as recurrent GBM subjects. Based on the discretized variables, subjects were then clustered

400   using hierarchical clustering with the Euclidean distance metrics.

Results

Marker expression differences between IDH1 mt and wt tumors

403   Univariate and multivariate analysis of biomarker expression in the treatment-naïve glioma cohort

404   showed significant differences in the mean expression of vimentin (p=0.0002), VEGFR2 (p=0.0002),

405   Nestin (p=0.003), Ki67 (p=0.006) and HLA1 (p=0.008) proteins between the IDHmt and IDHwt tumors

406   (**S6-A Fig.**). Three of these, VEGFR2, Vimentin and HLA1 were also included in the multi-variate model

407   using Random Forest which provided an AUC of 0.87 (error rate 5%) in predicting IDH mutation status

408   (**S6-B Fig.**). Since a majority of IDHmt tumors are derived from oligodendrogliomas which minimally

409   express vimentin and IDHmt tumors are known to have suppressed angiogenic pathways, differential

410   expression of VEGFR2 and vimentin between IDHmt and IDHwt is not surprising.

411

Cellular and genomic analysis shows cancer hallmark differences in

IDH1 mt vs wt tumors

Cellular differences in IDHmt vs wt tumors

415   In total, 24 markers across 85,000 cells from the 20 treatment-naive glioma cases underwent k-means

416   clustering. **Fig. 2** shows unsupervised clustering and segregation of the cells into 7 clusters; marker

417   intensity organized by cluster, IDH1 mutation and cancer hallmarks (invasion; energy metabolism;

418   angiogenesis; stem cells; immune response; proliferation; resisting cell death; DNA damage) and iron

419   metabolism. Relative biomarker intensities (compared to population mean) for each cluster are shown

420   in **S7 Fig.** Clusters 1 and 4 with above average expression of most hallmarks were composed of cells

421   from just two IDH1wt patients **(Fig. 2)**. Clusters 2 and 6 contained the largest numbers of cells (21.0%

422   and 21.9%, respectively, **S7 Fig.**) from the greatest number of cases (12 and 11 cases, respectively, **Fig.**

423   **2**), cluster 2 being dominantly composed of cells from IDH1wt tumors while cluster 6 contained cells

424   exclusively from IDHmt cases. Cluster 2 shows lower expression of γH2AX, Sox2, SMA, and Ncad and

425   higher expression of FTL and FTH1, while most other protein expression was near average of the all

426   clusters. Cluster 6 had lower expression of most of cancer hallmarks (**S7 Fig.**) and only pERK, CD31 and

427   Ncad had slightly above average expression. Clusters 5 with lower than average expression of all

428   hallmarks and cluster 7 with above average expression of most hallmarks were evenly occupied by cells

429   from both IDHwt and IDHmt cases. Notably, both angiogenesis and metabolism-related markers were

430   lower in IDH1mt cases, as was expression of antigen presenting machinery, i.e. HLA1, and invasion

431   markers collagen IV and vimentin. Lower expression of vimentin is consistent with IDH1 mutant tumors

432   originating from oligodendrocyte progenitor cells(45, 46), which minimally express vimentin.

433   Interestingly, IDHwt cells had higher expression of ferritin light and heavy chains, indicating increased

434   iron storage in these cells. Removal of free iron by enhanced iron storage has been implicating in

435   evading ferroptosis by cancer cells. A more in-depth analysis to this pathway in this cell cluster is

436   necessary to determine if evasion of ferroptosis is indeed driving the tumor growth in these patients.

437   **Fig. 3** shows two representative examples of IDHwt and mt tumor samples, with biomarker staining and

438   relative biomarker expression for clusters 2 and 6. Clustering of cells by expression of individual

439   hallmarks (angiogenesis, invasion and reprogramming cellular energetics) also showed significant

440   differences in cluster profiles and distribution of clusters among IDH mt and wt tumors (e.g. dominantly

20

441   higher representation of proangiogenic clusters in IDHwt tumors, **S8 Fig.**). Overall, similar staining

442   profiles and biomarker patterns in IDHmt vs wt cases were found in the recurrent GBM cohort.

443   **Fig. 2. Distribution and clustering of cells based on protein expression from all**

444   **treatment-naïve patients.** Unsupervised clustering of MxIF data revealed 7 distinct

445   subsets (clusters) of cells derived from all patients. Cluster 2 is dominated by IDH1wt

446   and Cluster 6 is dominated by IDH1mt cases. Clusters 1, 4 and 7 (which were less diverse

447   patient groups) show higher staining intensities of most MxIF markers (cancer

448   hallmarks) compared to Clusters 2, 5 and 6. Iron Metabolism hallmark was generally

449   high in Cluster 2, but low in Cluster 6.

450

451   **Fig. 3. IF images & Lolipop plots for Cell-DIVE cluster 2 and cluster 6 hallmarks**. MxIF

452   images for representative cases in Cluster 2 (A) and Cluster 6 (D), including a vH&E

453   image (top left), segmented image (top middle) showing individual cells, an image with

454   cluster assignment to individual cells (top right) and a number of single marker or multi-

455   marker overlays representing expression of different hallmark proteins (a: DNA breaks,

456   gH2AX. b: Iron metabolism; FTL, FTH1; c: Cell Death, Cleaved Caspase3; d: Proliferation,

457   EGFR, pERK, Ki67; e: Immune MHC1, PDL1; f: Stemness, Nestin, SOX2; g: Angiogenesis,

458   VEGFR2, SMA, S100A4, CD31; h & i: Metabolism, FASN overlaid on DAPI (h) & GSK3b,

459   PKM2, CA9 (i); j & k: Invasion, GFAP, Collagen IV (j) and Vimentin, Cofilin & NCad (k).

460   Panel B and Panel E show the protein expression profiles of individual clusters (2 & 6,

461   respectively); "lolipop" lines originate at the average expression of proteins in all cells

462   measured from all cases and dots reside at the expression of the proteins in the cluster.

463   Lines moving to the left show lower than average expression, while to the right show

464   higher than average expression. Cluster 2 (Panel C) and cluster 6 (Panel F) trend towards

465   separating cases by IDH1 mutation status. Specifically, Cluster 6, which shows a lower

466   than average expression of most hallmark proteins, is significantly positively correlated

467   to IDH1 mutation (Panel F); Cluster 2 cells with higher iron metabolism (FTL, FTH1) show

468   a trend towards lower representation in IDH1 mutant samples (Panel C). These positive

469   and negative correlations are even stronger when cluster representation in individual

470   cores is correlated to the overall patient status indicating that there is heterogeneity

471   within these tumors.

472

473   **Cell cluster alignment with IDH and other glioma related mutations**

474   **Fig. 4** shows cluster distribution aligned with IDH mutation status and the other most common

475   mutations in treatment-naïve glioma. In concordance with known biology, IDH1 mutations were found

476   to be mutually exclusive of EGFR and PTEN mutations (**Fig. 4, panel B**). IDH1mt samples appeared to be

477   more homogenous, particularly those with concurrent ATRX mutation, and were mostly dominated by

478   the cluster 6 cell phenotype (lower than average expression of most markers (panel A). Approx. 50% of

479   IDH1wt cases with EGFR amplification had a high proportion of cluster 2 cells (overall, average

480   biomarker expression, and lower DNA damage and stem cell markers, higher iron metabolism markers).

481   **Fig. 4. Cell cluster composition and Oncoprint of treatment naive gliomas.** For each

482   glioma case, Panel A portrays the fractional distribution of its cells within each of the 7

483   clusters. Panel B depicts the genomic profile of each glioma case.

484

485   **Cell cluster alignment with RNA expression and IDH status**

486   The degree to which single cell clusters agreed with deconvoluted, transcript-based cell class

487   assignments across treatment-naïve gliomas with IDHmt or wt was also evaluated. Based on the gene

22

488   expression data of all measured genes, we identified three cell classes using CellDistinguisher, each class

489   having 50 or more distinguisher genes **(S9 Fig.)**. Exceeding three classes resulted in a very short list of

490   distinguisher genes for some classes, which diminishes the utility of comparing behavior or functions

491   across the classes. Classes 2 & 3 were qualitatively similar to protein derived cell clusters 6 and 2

492   respectively. Ratios of the average staining intensities for 21 markers in clusters 6 and 2 were calculated

493   **(Fig. 5A).** The ratios of the expression values for the same 21 genes were compared between RNA

494   classes 2 and 3 **(Fig. 5B).** Fractional composition of IDHmt and wt cases within cell cluster 2 or 6 **(Fig. 5C)**

495   or within RNA class 2 or 3 **(Fig. 5D)** was determined. Consistent with earlier results, tumors dominated

496   by cluster 2 cells were more likely to be IDHwt, while cases with dominance of cluster 6 were mostly

497   IDH1mt. Similarly, the IDHwt tumors were mainly comprised of RNA class 3 markers while class 2 was

498   more abundant in the IDH1mt (**Fig. 5D**). IDH1wt tumors were enriched in class 3 cells (enriched in genes

499   related to the cancer hallmarks of inducing angiogenesis, enabling replicative immortality and evading

500   growth suppression), while the IDH1mt samples had a lower abundance of genes related to these cancer

501   hallmarks.

502   **Fig. 5. IDH1 mutation status drives cell phenotype at both the gene and the protein**

503   **level.** Ratios of the average staining intensities for 21 MxIF markers in clusters 6 and 2

504   were calculated (Panel A). Following deconvolution of the transcriptomes using

505   CellDistinguisher, RNA expression counts (FPKM) for the mRNAs were used to

506   distinguish "class types" (n=3) across the bulk sequenced specimens, then ratios of the

507   expression values for the same 21 genes compared between Class 2 and Class 3 (Panel

508   B. Fractional composition of each patient case within Cluster 2 or 6 (Panel C) or within

509   Class 2 or 3 (Panel D) was determined. Cases dominated by cells belonging to protein

510   cluster 2 were more likely to be found in IDH1 wild-type tumors, while cases for which

511   cells from cluster 6 dominated were mostly IDH1 mutated tumors (Panel C). Similarly,

23

512   the fractional composition of glioma cases comprised of gene expression class 3 were

513   present in higher proportions in IDH1 wild type samples, while class 2 cell types were

514   more abundant in the IDH1 mutant ones (Panel D). The distinguisher genes of class 3

515   were enriched in genes related to cancer hallmarks of "inducing angiogenesis",

516   "enabling replicative immortality" and "evading growth suppression" (see S4 Fig. and S2

517   Table).

518

519   We have found noteworthy similarity between the cell types and patient compositions identified from

520   the MxIF biomarker intensities and the gene expression data. Except for FASN, GSK3b and NCad, good

521   directional correlation was observed in differential protein and gene expression between cell clusters

522   and RNA classes in the IDH1mt and IDHwt populations (**Fig. 5**). Lack of concordance between H2AX

523   protein and transcript likely is due to staining intensity by anti-γH2AX antibody reporting only the post-

524   translationally phosphorylated form of the protein (instead of total protein, which the transcript count

525   would more reasonable reflect). The high concordant directionality of 17 of the 21 markers argues for

526   robustness of the biological inference that molecular features in cells from treatment-naïve gliomas are

527   related to IDH1 mutation status. We conclude that biomarker-based clusters 6 and 2 refer to the same

528   cells and/or processes as gene-expression-based classes 2 and 3. Although at individual gene levels,

529   mRNA and protein expression values don't evidence quantitative direct, strong correlation, our findings

530   indicate that looking at the behavior of cells at the gene set or pathway level can lead to consistent

531   patterns starting from different data types (47, 48).

532

533   **Intratumor and spatial heterogeneity**

534   In addition to the cell level protein expression and cell composition within the IDHmt and wt tumors, we

535   further investigated molecular and spatial heterogeneity of the biomarkers in each of the hallmark

24

536   categories. Examples of the heterogeneity metrics for the cell proliferation hallmark (comprising Ki67,

537   nestin and EGFR) in gliomas and recurrent GBMs are shown in **Fig. 6A,** which shows the discretized (high

538   (2), medium (1), low (0)) expression values for each marker, and corresponding color-coding for each

539   cell. Heterogeneity calculated from the distribution of these states in different tumors shows an inverse

540   correlation between molecular and spatial heterogeneity in both treatment-naïve glioma and recurrent

541   GBM cohorts. IDHwt tumors had higher molecular heterogeneity while IDHmt tumors were more

542   spatially heterogenous (S10 Fig.). Similar trends were present in both cohorts. **Fig. 6B** shows a scatter

543   plot of heterogeneity in the inducing angiogenesis hallmark with the range of spatial and molecular

544   heterogeneity metrics for gliomas and recurrent GBM samples, also encoded by IDHmt (red) and wt

545   (blue) status. Trends in heterogeneity of this hallmark were similar to those observed for the

546   proliferation hallmarks as well as activating invasion motility hallmark (S10 Fig.). No other significant

547   differences in heterogeneity were found.

548   **Fig. 6. Computed molecular and spatial heterogeneity metrics using the multi-omics**

549   **heterogeneity analysis (MOHA) tool.** The method first converts the continuous marker

550   intensity measures of each segmented cell into an ordinal value representing either a

551   high, medium, or low state. Panel (a) presents an example for the Sustaining

552   Proliferative Signaling cancer hallmark. This gene set is composed of three markers:

553   EGFR, Ki67, Nestin. The state of each of these markers can either be high (2), medium

554   (1), or low (0). Therefore, the three-marker gene set has 27 possible molecular states

555   presented in the color-coded legend (far left). The scatter plot (center) presents the

556   spatial and molecular heterogeneity of treatment naïve gliomas and recurrent GBM

557   samples. Images of tissues from four treatment naïve gliomas (A-D) and four recurrent

558   GBM (E-H) are presented with each segmented cell colored by their expressed

559   molecular state. The spatial state distributions of these eight samples are presented

560   above the scatter plot. For the 4-gene set "inducing angiogenesis" (SMA [ACTA2],

561   VEGFR2 [KDR], CD31 [PECAM1], and S100A4) hallmark, IDH1 mutation status

562   discriminates those cases with relatively lower molecular heterogeneity and relatively

563   higher spatial heterogeneity in grade III treatment-naïve glioma or recurrent

564   glioblastoma (panel b).

565

566

567   MR feature differences between IDH1 mutant and wildtype patients

568   Simple features derived from the MR images uncovered differences in discernable elements of brain

569   tumor dispersion from IDH1wt and IDH1mt patients. IDH1wt patients had larger enhancing cores

570   (feature "Normalized enhancing core volume"), but less contrast uptake in the peri-tumoral edema

571   regions (feature "Edema T1 post"). On the other hand, the IDH1mt patients lack a clearly defined

572   enhancing core, but have increased contrast uptake on the T1 post contrast MRI protocol in the peri-

573   tumoral edema region (**Fig. 7**). These trends were observed both in the treatment-naïve glioma as well

574   as the recurrent GBM, and are not surprising since the IDH1mt are known to have less contrast

575   enhancement than the IDH1wt (49).

576   **Fig. 7. MRI-derived features appear to differentiate patients that carry an IDH1**

577   **mutation (IDH1mt) and those that are wild type (IDH1wt), regardless if subjects are**

578   **treatment naïve or have recurring GBM.** T1w post contrast MRI for IDH1wt subjects

579   (a,e), and IDH1mt (b,f). The white outlines show the extent of the tumor as delineated

580   by the expert neuroradiologist (LW). (c,g) Across the two cohorts, a similar trend may be

581   notice when comparing the mean T1 post-contrast intensity signal in the peri-tumoral

582   edema region, suggesting an increase in enhancement in the IDH1mt in the peri-tumoral

583   edema region when compared to the IDH1wt (c and g). An opposite trend is observed

584   when comparing the normalized enhancing core volume across IDH1wt and IDH1mt (d

585   and h), indicating that subjects with IDH1 mutants have limited to no enhancement.

586   None of these comparisons reach statistical significance after multiple comparison

587   correction using false discovery rate.

588

589   Other intensity and volumetric features were evaluated on clinically important MRI protocols, e.g. ADC

590   or FLAIR, but they failed to show separation between IDH1 mutational status or a consistent trend

591   across the two cohorts. Thus, our analysis focuses on the normalized enhancing core volume –

592   measuring the enhancing core volume normalized to the entire tumor volume, and the T1w MRI post

593   contrast uptake in the peritumoral edema region. Statistical significance was not achieved for any

594   features after multiple comparison corrections likely due to the small number of patients in each cohort.

595   ## Multimodal data association

596   Unlike previous studies (27),(28-31) that focused on predicting IDH1 mutational status using MRI

597   features, we assessed the correlations of MRI features with genomic and proteomic markers within the

598   angiogenesis hallmark to characterize the differences between IDH1 mutational status. **S11 Fig.** shows

599   that larger enhancing cores are associated with higher RNA expression levels in the Inducing

600   Angiogenesis hallmark. A similar association is observed with the expression levels of protein markers,

601   i.e. S100A4 that is known to promote angiogenesis and metastasis development (50) , and VGFR2 that

602   plays a fundamental role in neovascularization (51). These found associations were consistent

603   regardless of the type of tumor, treatment naïve glioma or recurrent GBM.

604   When investigating multimodal associations (**Fig. 8**), we can also observe a consistent trend across the

605   two cohorts of patients. Not surprisingly, IDH1 mutations are found in lower grade tumors, younger

606   patients and have better overall survival. As also shown in **Fig. 7** and **S11 Fig.**, IDH1mt tumors have

607   smaller enhancing cores but more contrast uptake in the edema regions and show reduced expression

608   levels of RNA and protein from the Inducing Angiogenesis hallmark (**Fig. 8**, highlighted box). Of the five

609   angiogenesis hallmark cell clusters, cluster 4 (above average expression of VEGFR2, SMA and CD31) and

610   cluster 5 (above average expression of VEGFR2 and S100A4), which are characterized by higher

611   expression of angiogenesis markers, show low cell percentages in the subjects with IDH1 mutations. On

612   the other, the IDH1wt tumors are molecularly more diverse and show more heterogeneous multi-modal

613   variables, yet still a general trend of higher expression levels of RNA and protein markers involved in

614   inducing angiogenesis and reduced overall survival. Clusters with average (cluster 3) and lower than

615   average expression (clusters 1 & 2) were distributed among all patients, however, relative proportion of

616   these compared to the other two clusters was much higher in the IDHmt patients. Age, grade and

617   histology are confounding factors in the recurrent GBM progression cohort as IDH1mt tumors tend to

618   occur at younger age and are generally low grade oligodendrogliomas, however, as the similar trends

619   were apparent in the recurrent cohort, which are all grade IV GBMs, these observations probably reflect

620   differences in biology between the IDH1mt and IDH1wt tumors.

621   **Fig. 8. Comprehensive rendering of multi-scale measurements in gliomas**. Multiscale

622   modalities depicted include: 1) clinical information (red), 2) IDH1 Mutational status

623   (blue), 3) MRI derived variables (green), 4) RNA expression level of genes involved in the

624   Inducing Angiogenesis Hallmark (black), and 5) Multiplex Immunofluorescence

625   Angiogenesis markers or Cell clusters (magenta). The data is binned in low, medium and

626   high categories. Across the treatment-naïve gliomas (a) and the recurrent (post-

627   treatment) glioblastoma* (b) cohorts, it can be observed that subjects that carry the

628   IDH1 mutation have low angiogenesis according to RNA expression levels and

629   expression of S100A4 and VEGRF. The subjects also have high fraction of cells in clusters

630   1 and 2, and low fraction of cells in cluster 4 and 5 (**S8 Fig.**), cluster profiles of

631   angiogenesis clusters). Moreover, MR Images for the same subjects have lower

632   normalized enhancing cores volumes and measure higher intensities on T1 post

633   contrast. *Recurrent GBM (5 subjects are not shown since they were missing MxIF.)

634

Discussion

636   We deployed a multiscale workflow that accommodates biomedical imaging (multi-parameter MR

637   imaging) of glial tumors, *in situ* multiplex immunodetection of discrete biochemical functional states in

638   tissue sections from tumors, and next generation sequencing of DNA and RNA from those same tumors.

639   The data produced by each technology was post-processed to regions-of-interest and features (MRI),

640   molecular state assignments of individual cells in tissue (based on gene sets and signaling pathways

641   interrogated by specific antibodies), and molecular subtyping, pathway and hallmark mapping

642   (determined by mutations and cellular deconvolution from bulk RNA sequencing). A coherent picture of

643   enhanced angiogenesis in IDHwt tumors evident in non-invasive in vivo imaging features emerges from

644   the data derived from multiple platforms (genomic, proteomic and imaging) and scales from individual

645   proteins to cell clusters/states as well as bulk tumor. Results are consistent with known observations at

646   the molecular (suppression of proangiogenic markers in IDHmt tumors) and imaging scales (no or low

647   enhancement in IDHmt tumor), but now fill in the gaps on how the two are linked through the

648   intermediate scales of cellular states and their spatial organization. Multiplexed immunofluorescence

649   (MxIF) staining using 43 antibodies on individual tissue sections (duplicate punches in a tissue

650   microarray) afforded insight into the clustering of single cell functional states from 20 treatment-naïve

29

651   gliomas (grades 2 – 4) into 7 clusters. Discreet patterns of protein abundance across 7 hallmark

652   phenotypes and 2 biochemical signature events (iron metabolism and DNA damage) suggest that broad

653   segregation of such functional states may be associated with IDH1 mutation status. Among the more

654   robustly discriminating hallmarks between IDH1 wildtype from IDH1mutant gliomas is that of

655   angiogenesis. The enhancement patterns, specifically how much of the tumor enhances (assessed by the

656   "normalized enhancing core volume" feature) and the contrast uptake in the peri-tumoral edema region

657   (Edema T1 post intensity), appear to be consistently correlated with the IDH1 mutational status, a trend

658   that is conserved across the two independent cohorts we investigated. Our findings suggest that the

659   IDH1wt tumors have a more consistent enhancing pattern with a clearly defined enhancing rim and little

660   uptake elsewhere. On the other hand, the IDH1mt tumors have a diffuse appearance on MRI without a

661   well-defined enhancing rim and with higher uptake in the edema region, on account of infiltrating cells.

662   Previous studies have linked poor survival with the peritumoral edema volume (52) and tumor volume

663   (27). Moreover, IDH1mt tumors are known to have less edema (49). From the richness of the molecular

664   heterogeneity portrayed from MxIF scoring, comparing the functional states of adjacent cells (whether

665   they are similar or dissimilar) affords a calculation of spatial heterogeneity across the different hallmark

666   phenotypes. Here we find the unanticipated segregation of both treatment-naïve gliomas as well as

667   recurrent glioblastoma based on IDH1 mutation status within hallmarks of "invasion motility",

668   "proliferative signaling", and "angiogenesis". The genomic profiling depicted what is already known

669   about glial tumors, (the mutual exclusivity of IDH1 mutations with EGFR and PTEN mutations, the co-

670   existence of ATRX mutations only within a subset of IDH1 low grade tumors, etc), but also revealed the

671   heretofore unknown frequent, diminished molecular heterogeneity of IDH1mt low grade tumors.

672   Removal of free iron by enhanced iron storage has been implicated in evading ferroptosis by cancer cells

673   (34, 35). Cluster 2, which was highly represented in IDH1wt tumors showed an increased expression of

674   iron storage markers (FTL and FTH1) and decreased expression of γH2AX, a marker of DNA breaks (**S7**

30

675   **Fig.**). This is consistent with increased sequestration of iron, making it unavailable for oxidative DNA

676   damage leading to evasion of ferroptosis. A more in-depth analysis of this pathway that includes iron

677   transport, storage and utilization is necessary to determine if evasion of ferroptosis is indeed driving the

678   tumor growth in these patients (53, 54). Inter- and intra- tumoral molecular heterogeneity is a well-

679   recognized feature of GBM (6, 55, 56) and is believed to be the main reason behind treatment failure.

680   Emergence of several single cell analysis platforms has fueled the investigations of intra-tumoral

681   heterogeneity of glioma (17, 57-59) , including tumor-stromal cell interactions (60, 61) as well as

682   interactions between the diverse tumor cell populations (62, 63). Importance of the intercellular

683   interactions among heterogenous tumor cell population is highlighted by the observations of Inda et. al.

684   (62) that EGFRmt cells that are far outnumbered by the EGFRwt population drive enhanced proliferation

685   of these cells by paracrine signaling thereby driving tumor growth. Thus, tools to evaluate molecular

686   and spatial heterogeneity and cell-cell interactions are likely to unravel heretofore unknown

687   mechanisms that drive tumor growth and/or treatment failure. IDH mutation induced suppression of

688   immune response has also been noted previously, however, it has been linked to decreased expression

689   of effector T cell response related genes (64) . Weather this in turn affects the expression of HLA1 in

690   IDHmt tumors is not known.

691

692   ## Study limitations

693   The key limitations of this study include small sample size, lack of registration of sample derived for

694   molecular analysis to MR images and a limited number of markers representing different hallmarks. The

695   intent of this study was not to generate a diagnostic signature but to evaluate correlation between

696   imaging and molecular features at the hallmark level and to generate a work flow for integrating

697   multiscale multiparametric data to study disease biology. While the sample size (n=20) in the

31

698   treatment-naïve glioma cohort was limited, the fact that similar cell clusters existed in another cohort

699   (recurrent GBM) and the correlations between MR and molecular features of angiogenesis hallmark

700   hold for both cohorts is encouraging. Having developed methods to integrate and evaluate such a

701   complex data set, we are in the process of designing a more focused study to interrogate the biology of

702   a specific molecular subtype of GBM that will consider and address the aforementioned shortcomings.

Acknowledgements

706

References

708   1.   Ostrom QT, Gittleman H, Truitt G, Boscia A, Kruchko C, Barnholtz-Sloan JS. CBTRUS Statistical

709   Report: Primary Brain and Other Central Nervous System Tumors Diagnosed in the United States in

710   2011-2015. Neuro Oncol. 2018;20(suppl_4):iv1-iv86.

711   2.   Brennan CW, Verhaak RG, McKenna A, Campos B, Noushmehr H, Salama SR, et al. The somatic

712   genomic landscape of glioblastoma. Cell. 2013;155(2):462-77.

713   3.   Cancer Genome Atlas Research N, Brat DJ, Verhaak RG, Aldape KD, Yung WK, Salama SR, et al.

714   Comprehensive, Integrative Genomic Analysis of Diffuse Lower-Grade Gliomas. N Engl J Med.

715   2015;372(26):2481-98.

716   4.   Ceccarelli M, Barthel FP, Malta TM, Sabedot TS, Salama SR, Murray BA, et al. Molecular Profiling

717   Reveals Biologically Discrete Subsets and Pathways of Progression in Diffuse Glioma. Cell.

718   2016;164(3):550-63.

719   5.   Consortium G. Glioma through the looking GLASS: molecular evolution of diffuse gliomas and

720   the Glioma Longitudinal Analysis Consortium. Neuro Oncol. 2018;20(7):873-84.

721   6.   Cancer Genome Atlas Research N. Comprehensive genomic characterization defines human

722   glioblastoma genes and core pathways. Nature. 2008;455(7216):1061-8.

723   7.   Phillips HS, Kharbanda S, Chen R, Forrest WF, Soriano RH, Wu TD, et al. Molecular subclasses of

724   high-grade glioma predict prognosis, delineate a pattern of disease progression, and resemble stages in

725   neurogenesis. Cancer Cell. 2006;9(3):157-73.

726   8.   Bhat KPL, Balasubramaniyan V, Vaillant B, Ezhilarasan R, Hummelink K, Hollingsworth F, et al.

727   Mesenchymal differentiation mediated by NF-kappaB promotes radiation resistance in glioblastoma.

728   Cancer Cell. 2013;24(3):331-46.

729   9.   Hegi ME, Diserens AC, Godard S, Dietrich PY, Regli L, Ostermann S, et al. Clinical trial

730   substantiates the predictive value of O-6-methylguanine-DNA methyltransferase promoter methylation

731   in glioblastoma patients treated with temozolomide. Clin Cancer Res. 2004;10(6):1871-4.

732   10.   Noushmehr H, Weisenberger DJ, Diefes K, Phillips HS, Pujara K, Berman BP, et al. Identification

733   of a CpG island methylator phenotype that defines a distinct subgroup of glioma. Cancer Cell.

734   2010;17(5):510-22.

735   11.   Yan H, Parsons DW, Jin G, McLendon R, Rasheed BA, Yuan W, et al. IDH1 and IDH2 mutations in

736   gliomas. N Engl J Med. 2009;360(8):765-73.

737   12.   Cimino PJ, Zager M, McFerrin L, Wirsching HG, Bolouri H, Hentschel B, et al. Multidimensional

738   scaling of diffuse gliomas: application to the 2016 World Health Organization classification system with

739   prognostically relevant molecular subtype discovery. Acta Neuropathol Commun. 2017;5(1):39.

740   13.   Louis DN, Perry A, Reifenberger G, von Deimling A, Fig.arella-Branger D, Cavenee WK, et al. The

741   2016 World Health Organization Classification of Tumors of the Central Nervous System: a summary.

742   Acta Neuropathol. 2016;131(6):803-20.

743   14.   Aum DJ, Kim DH, Beaumont TL, Leuthardt EC, Dunn GP, Kim AH. Molecular and cellular

744   heterogeneity: the hallmark of glioblastoma. Neurosurg Focus. 2014;37(6):E11.

33

745   15.   Sottoriva A, Spiteri I, Piccirillo SG, Touloumis A, Collins VP, Marioni JC, et al. Intratumor

746   heterogeneity in human glioblastoma reflects cancer evolutionary dynamics. Proc Natl Acad Sci U S A.

747   2013;110(10):4009-14.

748   16.   Kumar A, Boyle EA, Tokita M, Mikheev AM, Sanger MC, Girard E, et al. Deep sequencing of

749   multiple regions of glial tumors reveals spatial heterogeneity for mutations in clinically relevant genes.

750   Genome Biol. 2014;15(12):530.

751   17.   Patel AP, Tirosh I, Trombetta JJ, Shalek AK, Gillespie SM, Wakimoto H, et al. Single-cell RNA-seq

752   highlights intratumoral heterogeneity in primary glioblastoma. Science. 2014;344(6190):1396-401.

753   18.   Furnari FB, Cloughesy TF, Cavenee WK, Mischel PS. Heterogeneity of epidermal growth factor

754   receptor signalling networks in glioblastoma. Nat Rev Cancer. 2015;15(5):302-10.

755   19.   Morokoff A, Ng W, Gogos A, Kaye AH. Molecular subtypes, stem cells and heterogeneity:

756   Implications for personalised therapy in glioma. J Clin Neurosci. 2015;22(8):1219-26.

757   20.   Ryu YJ, Choi SH, Park SJ, Yun TJ, Kim JH, Sohn CH. Glioma: application of whole-tumor texture

758   analysis of diffusion-weighted imaging for the evaluation of tumor heterogeneity. PLoS One.

759   2014;9(9):e108335.

760   21.   Gerdes MJ, Sevinsky CJ, Sood A, Adak S, Bello MO, Bordwell A, et al. Highly multiplexed single-

761   cell analysis of formalin-fixed, paraffin-embedded cancer tissue. Proc Natl Acad Sci U S A.

762   2013;110(29):11982-7.

763   22.   Kiefer J, Sara N, Graf JL, Kodira C, Ginty F, Newberg L, et al. Hallmarks of Cancer Gene Set

764   Annotation2017.

765   23.   Bai HX, Lee AM, Yang L, Zhang P, Davatzikos C, Maris JM, et al. Imaging genomics in cancer

766   research: limitations and promises. Br J Radiol. 2016;89(1061):20151030.

767   24.   Ellingson BM. Radiogenomics and imaging phenotypes in glioblastoma: novel observations and

768   correlation with molecular characteristics. Curr Neurol Neurosci Rep. 2015;15(1):506.

34

769   25.   Pinker K, Shitano F, Sala E, Do RK, Young RJ, Wibmer AG, et al. Background, current role, and

770   potential applications of radiogenomics. J Magn Reson Imaging. 2018;47(3):604-20.

771   26.   Sala E, Mema E, Himoto Y, Veeraraghavan H, Brenton JD, Snyder A, et al. Unravelling tumour

772   heterogeneity using next-generation imaging: radiomics, radiogenomics, and habitat imaging. Clin

773   Radiol. 2017;72(1):3-10.

774   27.   Carrillo JA, Lai A, Nghiemphu PL, Kim HJ, Phillips HS, Kharbanda S, et al. Relationship between

775   tumor enhancement, edema, IDH1 mutational status, MGMT promoter methylation, and survival in

776   glioblastoma. AJNR Am J Neuroradiol. 2012;33(7):1349-55.

777   28.   Park YW, Han K, Ahn SS, Bae S, Choi YS, Chang JH, et al. Prediction of IDH1-Mutation and

778   1p/19q-Codeletion Status Using Preoperative MR Imaging Phenotypes in Lower Grade Gliomas. AJNR

779   Am J Neuroradiol. 2018;39(1):37-42.

780   29.   Su CQ, Lu SS, Zhou MD, Shen H, Shi HB, Hong XN. Combined texture analysis of diffusion-

781   weighted imaging with conventional MRI for non-invasive assessment of IDH1 mutation in anaplastic

782   gliomas. Clin Radiol. 2018.

783   30.   Li ZC, Bai H, Sun Q, Zhao Y, Lv Y, Zhou J, et al. Multiregional radiomics profiling from

784   multiparametric MRI: Identifying an imaging predictor of IDH1 mutation status in glioblastoma. Cancer

785   Med. 2018;7(12):5999-6009.

786   31.   Chang K, Bai HX, Zhou H, Su C, Bi WL, Agbodza E, et al. Residual Convolutional Neural Network

787   for the Determination of IDH Status in Low- and High-Grade Gliomas from MR Imaging. Clin Cancer Res.

788   2018;24(5):1073-81.

789   32.   Kickingereder P, Sahm F, Radbruch A, Wick W, Heiland S, Deimling A, et al. IDH mutation status

790   is associated with a distinct hypoxia/angiogenesis transcriptome signature which is non-invasively

791   predictable with rCBV imaging in human glioma. Sci Rep. 2015;5:16238.

792   33.   Byron SA, Tran NL, Halperin RF, Phillips JJ, Kuhn JG, de Groot JF, et al. Prospective Feasibility Trial

793   for Genomics-Informed Treatment in Recurrent and Progressive Glioblastoma. Clin Cancer Res.

794   2018;24(2):295-305.

795   34.   Hangauer MJ, Viswanathan VS, Ryan MJ, Bole D, Eaton JK, Matov A, et al. Drug-tolerant persister

796   cancer cells are vulnerable to GPX4 inhibition. Nature. 2017;551(7679):247-50.

797   35.   Viswanathan VS, Ryan MJ, Dhruv HD, Gill S, Eichhoff OM, Seashore-Ludlow B, et al. Dependency

798   of a therapy-resistant state of cancer cells on a lipid peroxidase pathway. Nature. 2017;547(7664):453-7.

799   36.   Xie Y, Hou W, Song X, Yu Y, Huang J, Sun X, et al. Ferroptosis: process and function. Cell Death

800   Differ. 2016;23(3):369-79.

801   37.   Padfield D, Rittscher J, Roysam B. Coupled minimum-cost flow cell tracking for high-throughput

802   quantitative analysis. Med Image Anal. 2011;15(4):650-68.

803   38.   Halperin RF, Carpten JD, Manojlovic Z, Aldrich J, Keats J, Byron S, et al. A method to reduce

804   ancestry related germline false positives in tumor only somatic variant calling. BMC Med Genomics.

805   2017;10(1):61.

806   39.   Aran D, Butte AJ. Digitally deconvolving the tumor microenvironment. Genome Biol.

807   2016;17(1):175.

808   40.   Teschendorff AE, Breeze CE, Zheng SC, Beck S. A comparison of reference-based algorithms for

809   correcting cell-type heterogeneity in Epigenome-Wide Association Studies. BMC Bioinformatics.

810   2017;18(1):105.

811   41.   Newberg LA, Chen X, Kodira CD, Zavodszky MI. Computational de novo discovery of

812   distinguishing genes for biological processes and cell types in complex tissues. PLoS One.

813   2018;13(3):e0193067.

814   42.   Gaujoux R, Seoighe C. CellMix: a comprehensive toolbox for gene expression deconvolution.

815   Bioinformatics. 2013;29(17):2211-2.

816   43.   Graf JF, Zavodszky MI. Characterizing the heterogeneity of tumor tissues from spatially resolved

817   molecular measures. PLoS One. 2017;12(11):e0188878.

818   44.   Menze BH, Jakab A, Bauer S, Kalpathy-Cramer J, Farahani K, Kirby J, et al. The Multimodal Brain

819   Tumor Image Segmentation Benchmark (BRATS). IEEE Trans Med Imaging. 2015;34(10):1993-2024.

820   45.   Alcantara Llaguno SR, Wang Z, Sun D, Chen J, Xu J, Kim E, et al. Adult Lineage-Restricted CNS

821   Progenitors Specify Distinct Glioblastoma Subtypes. Cancer Cell. 2015;28(4):429-40.

822   46.   Alcantara Llaguno SR, Xie X, Parada LF. Cell of Origin and Cancer Stem Cells in Tumor Suppressor

823   Mouse Models of Glioblastoma. Cold Spring Harb Symp Quant Biol. 2016;81:31-6.

824   47.   Akan P, Alexeyenko A, Costea PI, Hedberg L, Solnestam BW, Lundin S, et al. Comprehensive

825   analysis of the genome transcriptome and proteome landscapes of three tumor cell lines. Genome Med.

826   2012;4(11):86.

827   48.   Maier T, Guell M, Serrano L. Correlation of mRNA and protein in complex biological samples.

828   FEBS Lett. 2009;583(24):3966-73.

829   49.   Wasserman JK, Nicholas G, Yaworski R, Wasserman AM, Woulfe JM, Jansen GH, et al.

830   Radiological and pathological features associated with IDH1-R132H mutation status and early mortality

831   in newly diagnosed anaplastic astrocytic tumours. PLoS One. 2015;10(4):e0123890.

832   50.   Semov A, Moreno MJ, Onichtchenko A, Abulrob A, Ball M, Ekiel I, et al. Metastasis-associated

833   protein S100A4 induces angiogenesis through interaction with Annexin II and accelerated plasmin

834   formation. J Biol Chem. 2005;280(21):20833-41.

835   51.   Basagiannis D, Zografou S, Murphy C, Fotsis T, Morbidelli L, Ziche M, et al. VEGF induces

836   signalling and angiogenesis by directing VEGFR2 internalisation through macropinocytosis. J Cell Sci.

837   2016;129(21):4091-104.

838   52.   Wu CX, Lin GS, Lin ZX, Zhang JD, Liu SY, Zhou CF. Peritumoral edema shown by MRI predicts poor

839   clinical outcome in glioblastoma. World J Surg Oncol. 2015;13:97.

840   53.   Tong L, Yi L, Liu P, Abeysekera IR, Hai L, Li T, et al. Tumour cell dormancy as a contributor to the

841   reduced survival of GBM patients who received standard therapy. Oncol Rep. 2018;40(1):463-71.

842   54.   Wu T, Li Y, Liu B, Zhang S, Wu L, Zhu X, et al. Expression of Ferritin Light Chain (FTL) Is Elevated in

843   Glioblastoma, and FTL Silencing Inhibits Glioblastoma Cell Proliferation via the GADD45/JNK Pathway.

844   PLoS One. 2016;11(2):e0149361.

845   55.   Friedmann-Morvinski D. Glioblastoma heterogeneity and cancer cell plasticity. Crit Rev Oncog.

846   2014;19(5):327-36.

847   56.   Meyer M, Reimand J, Lan X, Head R, Zhu X, Kushida M, et al. Single cell-derived clonal analysis of

848   human glioblastoma links functional and genomic heterogeneity. Proc Natl Acad Sci U S A.

849   2015;112(3):851-6.

850   57.   Chen KH, Boettiger AN, Moffitt JR, Wang S, Zhuang X. RNA imaging. Spatially resolved, highly

851   multiplexed RNA profiling in single cells. Science. 2015;348(6233):aaa6090.

852   58.   Shah S, Lubeck E, Zhou W, Cai L. In Situ Transcription Profiling of Single Cells Reveals Spatial

853   Organization of Cells in the Mouse Hippocampus. Neuron. 2016;92(2):342-57.

854   59.   Stahl PL, Salmen F, Vickovic S, Lundmark A, Navarro JF, Magnusson J, et al. Visualization and

855   analysis of gene expression in tissue sections by spatial transcriptomics. Science. 2016;353(6294):78-82.

856   60.   Chen Z, Hambardzumyan D. Immune Microenvironment in Glioblastoma Subtypes. Front

857   Immunol. 2018;9:1004.

858   61.   Dey MF, H.; Heimberger, A.B. The Role of Glioma Microenvironment in Immune Modulation:

859   Potential Targets for Intervention. Letters in Drug Design & Discovery. 2006;3(7):11.

860   62.   Inda MM, Bonavia R, Mukasa A, Narita Y, Sah DW, Vandenberg S, et al. Tumor heterogeneity is

861   an active process maintained by a mutant EGFR-induced cytokine circuit in glioblastoma. Genes Dev.

862   2010;24(16):1731-45.

38

863   63.   Inda MM, Bonavia R, Seoane J. Glioblastoma multiforme: a look inside its heterogeneous nature.

864   Cancers (Basel). 2014;6(1):226-39.

865   64.   Kohanbash G, Carrera DA, Shrivastav S, Ahn BJ, Jahan N, Mazor T, et al. Isocitrate

866   dehydrogenase mutations suppress STAT1 and CD8+ T cell accumulation in gliomas. J Clin Invest.

867   2017;127(4):1425-37.

868   # Supporting Information

869

870   **S1 Table. Detailed patient characteristics and datasets for treatment naïve glioma cohort**

871

872   **S2 Table. Detailed patient characteristics and datasets for recurrent GBM cohort**

873

874   **S3 Table: Antibody information and staining sequence**

875

876   **S4 Table: Min and max number of cells per core in glioma and recurrent GBM TMAs**

877

878   **S1 Fig. Multiplexed immunofluorescence (MxIF) workflow**

879   The Cell DIVE MxIF workflow involves repeated cycles of staining, imaging and signal inactivation (panel

880   A), following slide clearing and antigen retrieval. Prior to antibody staining, tissue is stained with DAPI

881   and imaged in all channels of interest to record background autofluorescence (AF) of the tissue.

882   Following background imaging, tissue is stained with 2-3 antibodies and reimaged to capture antigen-

883   specific signal and then undergoes a dye inactivation step to remove the signal. The slide is re-imaged to

884   measure background fluorescence intensity. These cycles are repeated multiple times until all targets of

885   interest have been imaged. Panel 2 shows various image processing steps prior to generating single cell

886   data. Some of these are performed during imaging itself while others are performed post image

887   acquisition. The steps include, illumination correction, to correct for uneven illumination across the

888   FOV, registration of images from all rounds (using DAPI signal from each round) and tissue AF removal.

889   Panel C: Staining intensity of various cellular and subcellular markers is used to generate cellular

890   segmentation masks. Segmented images are compared with real or virtual H&Es (generated from DAPI

891   stained background images at the beginning of multiplexing) by a trained biologist or pathologist, and

892   images with poor segmentation are removed from analysis. In parallel, marker staining is evaluated by

893   reviewing AF removed images and markers that failed to stain or images with large artefacts are

894   removed from analysis. Marker expression is quantified at cellular and subcellular compartments and

895   data is generated in an easy to use .csv or Excel format which is then analyzed by a variety of different

896   tools/approaches including simple statistical correlations, cluster analysis as well as heterogeneity

897   analysis.

898

899   **S2 Fig. Antibody validation workflow**

900   A typical antibody validation workflow: Starting with literature reports to identify antibody clones

901   previously used for IHC on FFPE tissue, 3 or more clones per target are identified and evaluated for

902   sensitivity and specificity of the signal on a multi-tissue array (TMA) comprising all major tumor types

903   and corresponding normal tissues. The down-selected antibody is conjugated with CY3, Cy5 or Cy7 at 2

904   different dye/protein ratio and conjugates validated by staining comparison with unconjugated primary

905   on serial sections of the same TMA. The down-selected conjugate is tested at different concentrations

906   on a TMA with tumor tissue of interest to determine the optimal concentration for staining. In parallel,

907   a set of TMA serial sections are pre-treated with different rounds of bleaching and evaluated for

908   bleaching solution's effect on antigen of interest by comparing the staining among this set. Antigens

909   with discernible effects are prioritized for staining early in the sequence, immediately after primary

910   secondary staining of targets which failed to conjugate.

911

912   **S3 Fig. Marker Staining quality assessment**

913   A: Marker staining performance in each cohort (True-positive, False-negative), staining round,

914   subcellular location used for analysis and gene symbol, B: examples of quantitative FOV level correlation

915   of marker intensities on replicate slides, C: Examples of fluorescence image overlays of various hallmark

916   markers showing heterogeneity of expression in astrocytoma.

917

918   **S4 Fig. Number of segmented cells in serial sections**

919   High correlation in number of segmented cells was observed between serial sections, particularly for the

920   treatment naïve glioma cohort and two out of three sections of the recurrent GBM cohort.

921

922   **S5 Fig. Example workflow for calculating cell molecular state and cell spatial heterogeneity**

923   Example of how molecular state and cell spatial heterogeneity metrics are calculated, using EGFR as an

924   example. A. Segmentation of cells using DAPI staining and generation of nuclear and extra-nuclear

925   masks; B. EGFR fluorescence intensity is quantified for each cell and discretized as low, moderate, and

926   high. The different levels of cell expression are shown as red (high), green (moderate) or blue (low). C.

927   For each cell (I through v in this cartoon), adjacent neighboring (touching) cells are counted, and their

928   Spatial State is used to sum the Spatial Heterogeneity.

929

930   **S6 Fig. Uni- (A) and multi-variate (B) analysis of biomarker expression and overall survival as a**

931   **function of IDH mutation status**

932   A. Differences in individual biomarker expression and survival of IDHmt and IDHwt patients. B. A

933   predictive multivariate model of IDH mutation status.

934

935   **S7 Fig. Lollipop plots for biomarker expression in each cluster, relative to population median**

936   Protein expression profiles of individual clusters plotted relative to median expression in the whole

937   population. Solid circles represent the average expression in the cluster while direction and length of the

938   lollipop shows difference in expression relative to population median (left-lower, right-higher).

939

940   **S8 Fig. Cell clusters based on angiogenesis hallmark proteins**

941   Unsupervised clustering of cells using angiogenesis hallmark proteins identified a 5 cluster set. Clusters

942   with lower than average hallmark protein expression (1 & 2) are highly represented in samples with

943   IDH1 mutation. Cluster 4 & 5 with higher expression are proportionally more abundant in IDH1wt

944   samples.

945

946   **S9 Fig. Abundance of distinguisher genes (mRNA)/class per patient**

947   A: Relative proportion of cells belonging to different CellDistinguisher classes in each sample. Class 3 is

948   highly represented in IDHwt samples. B: shows relative abundance of distinguisher genes grouped by

949   hallmarks in individual classes.

950

951   **S10 Fig. Molecular and spatial heterogeneity in grade III gliomas and recurrent GBM IDHwt and IDHmt**

952   **tumors**

953   Molecular and spatial heterogeneity in grade III gliomas and recurrent GBM IDHwt and IDHmt tumors

954   according to the following hallmarks: Invasion and Motility, Cell Proliferative Signaling and Inducing

955   Angiogenesis.

956

957   **S11 Fig. Differences in MR features across the population range of RNA and protein marker**

958   **expression for angiogenesis**

959   Correlation between Normalized enhancing core volume (derived from MRI) and Angiogenesis

960   estimated from (a,d) RNA expression levels, and, based on multiplex immunofluorescence (MxIF)

961   angiogenesis markers (b, e) S100A4 and (c,f) VEGFR2; (a-c) shows the plots on Cohort 1 (CW Glioma,

962   treatment naive) while (d-f) show cohort 2 (UCSF, recurrent GBM). A progressive increasing trend may

963   be observed in both cohorts when examining the normalized enhancing core volume for low, medium

964   and high angiogenesis. The trends across the enhancement ratio are also conserved when comparing

965   RNA with MxIF Angiogenesis. None of these comparisons reach statistical significance after multiple

966   comparison correction using false discovery rate.

967

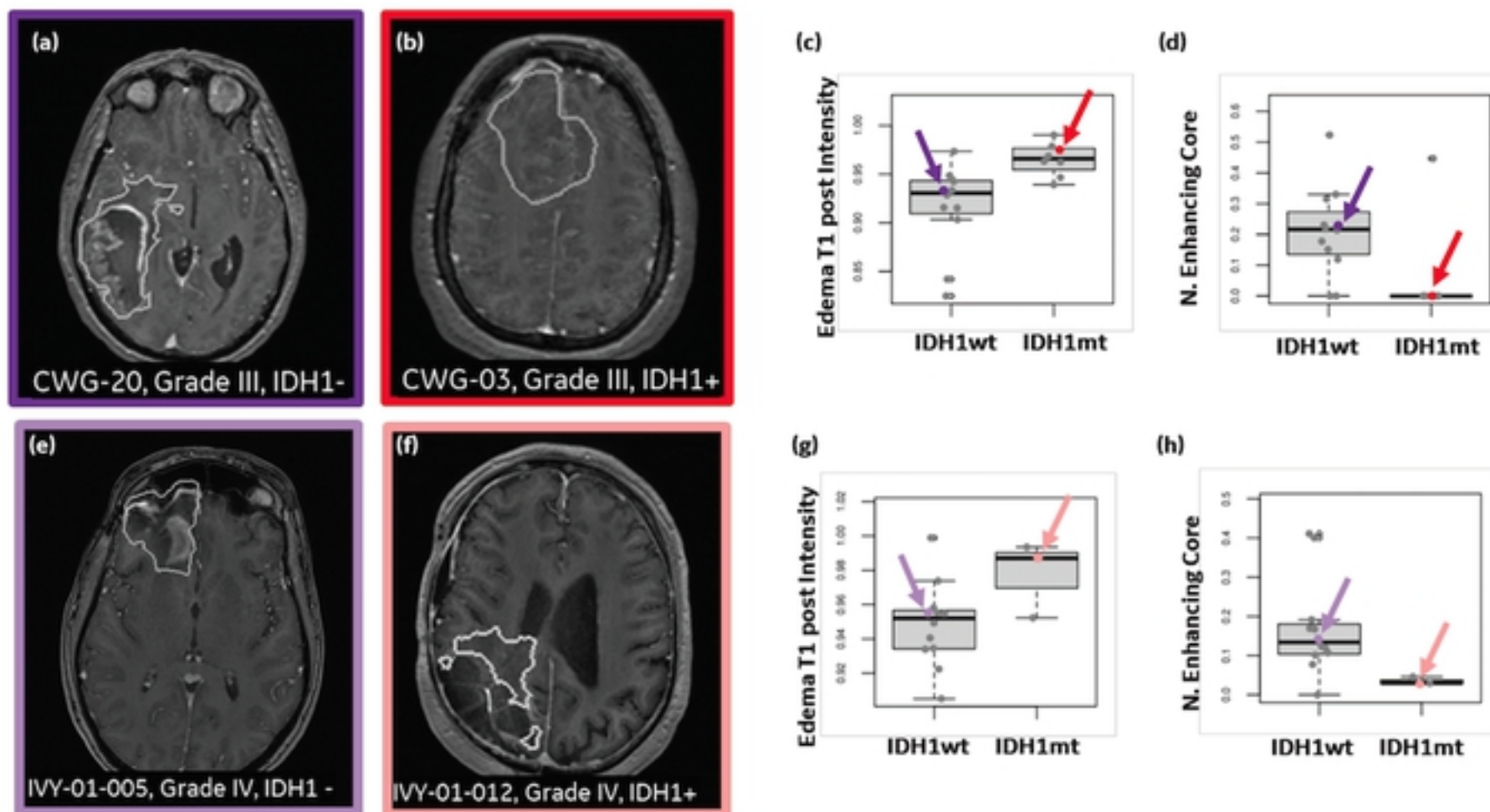Figure 7: MRI-derived features T1 edema and enhancement in IDH1wt and IDHmt tumors

Figure 7

Paper Figures:

Table 1: Patient characteristics summary
Figure 1: Multimodal data workflow
Figure 2: Distribution and clustering of cells based on protein expression from all treatment-naïve patients.
Figure 3: Cluster 2 and 6 profiles and example images for selected biomarkers in IDHwt and IDHmt tumors
Figure 4: Cell cluster composition and oncoprint of treatment naive gliomas
Figure 5. Correlation between IDH1 mutation status and cell phenotype at both gene and protein level.
Figure 6: Computed molecular and spatial heterogeneity metrics using the multi-omics heterogeneity analysis (MOHA) tool
Figure 7: MRI-derived features T1 edema and enhancement in IDH1wt and IDHmt tumors
Figure 8: Multiscale modality integration including IDH1 mutation, clinical data, survival, RNA expression (angiogenesis markers), protein expression and cell clusters

Paper Figures List

Table 1: Patient Characteristics

Cohort	Treatment naïve primary glioma patients	Recurrent/Refractory GBM patients
Patient number	20	16
Median (range) age at diagnosis (years)	57 (26-77)	51 (29-66)
Gender		
Male	12	12
Female	8	4
Ethnicity		
Caucasian	18	15
Hispanic, Asian, African American	0, 1, 1	1, 0, 0
Histologic Grade		
II	5	-
III	7	-
IV	8	16
IDH1/2 Mutation status		
Mutant (IDH1 R132H)	8	3
Wildtype	12	13
1p19q codeletion		
Codeletion	4	-
Non-codeletion	16	-
Median (range) Survival (days)		
Grade II	1120 (420-2326)	
Grade III	487 (370-2964)	
Grade IV (GBM)	438 (222-541)	1031 (396-3771)

Table 1

Figure 6: Computed molecular and spatial heterogeneity metrics using the multi-omics heterogeneity analysis (MOHA) tool

(a) Heterogeneity of cell proliferative markers
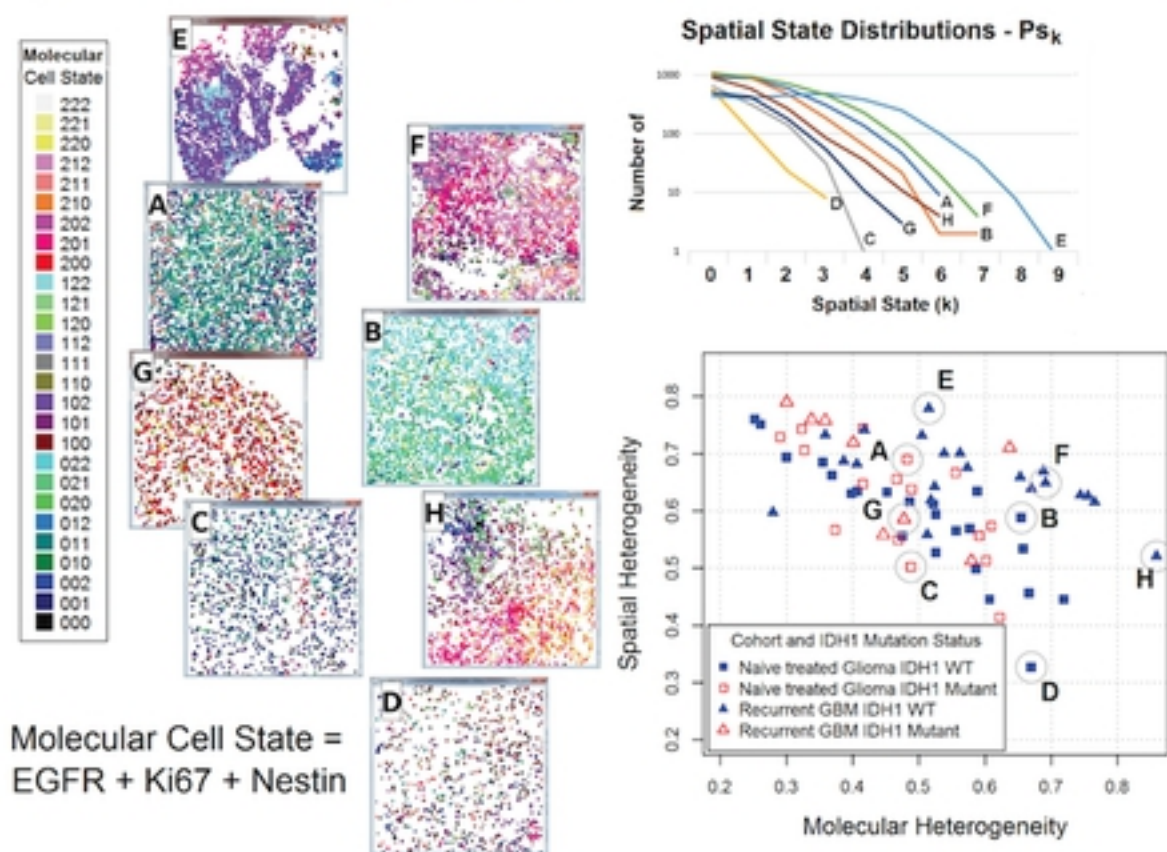
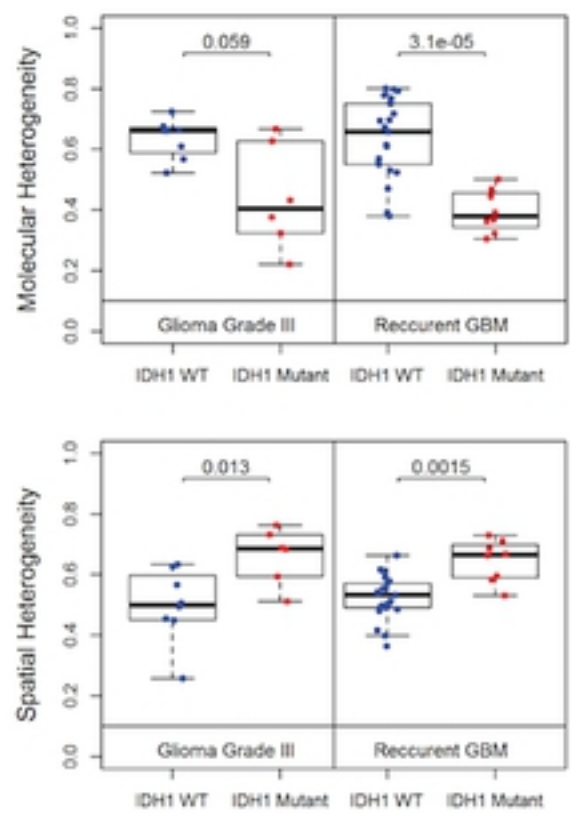(b) Heterogeneity of inducing angiogenesis

Figure 6

Figure 1: Overall workflow for generating multi-scale, multiparametric data, extraction of features and/or conversion to higher scales and analysis approaches
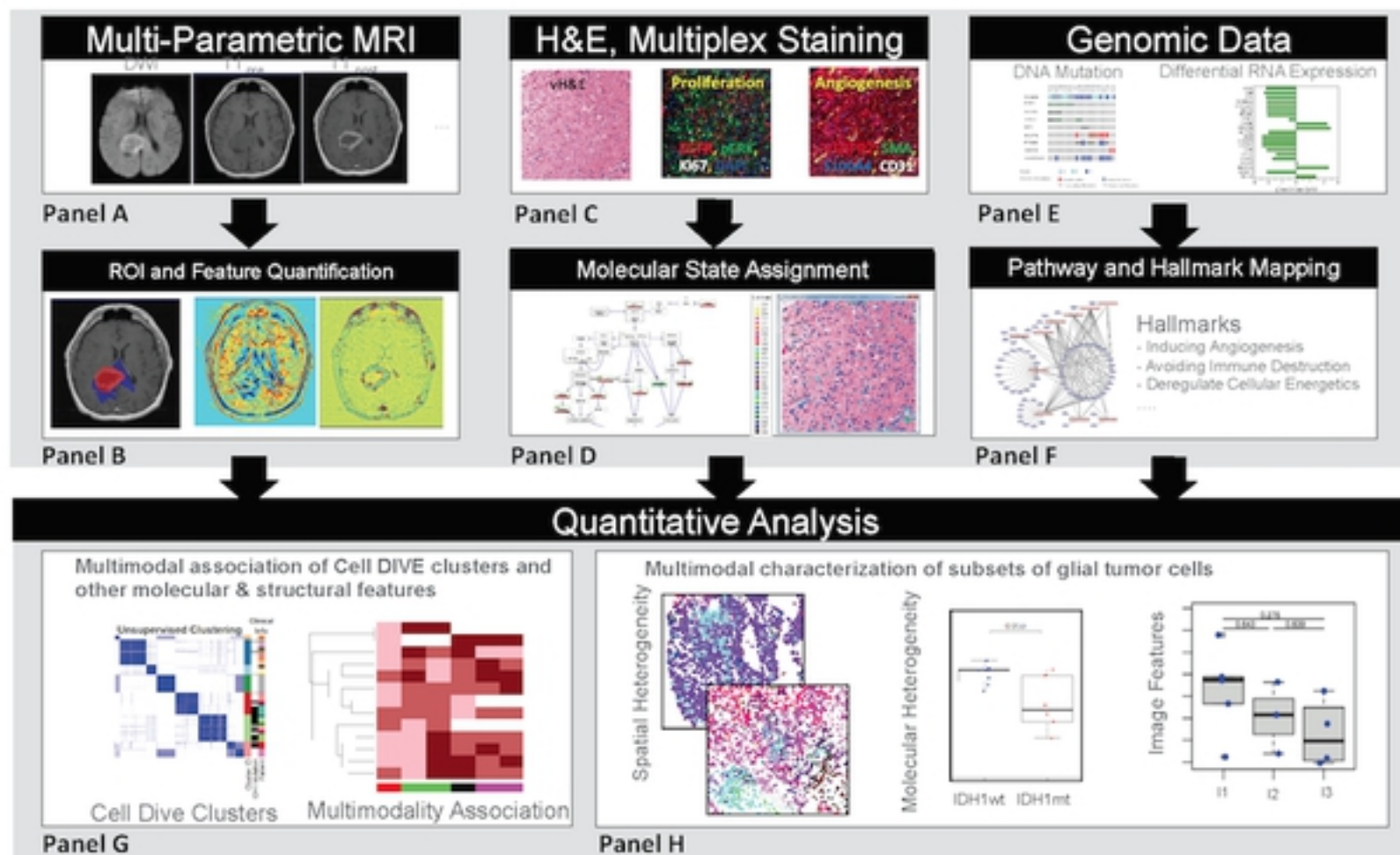

Panel A — Multi-Parametric MRI

Panel C — H&E, Multiplex Staining

Panel E — Genomic Data

Panel B — ROI and Feature Quantification

Panel D — Molecular State Assignment

Panel F — Pathway and Hallmark Mapping

Quantitative Analysis

Panel G — Multimodal association of Cell DIVE clusters and other molecular & structural features

Panel H — Multimodal characterization of subsets of glial tumor cells

Figure 1

Figure 3: Cluster 2 and 6 profiles and example images for selected biomarkers in IDHwt and IDHmt tumors

Sample with cluster 2 dominant Astrocytoma grade III, IDHwt

A

B. Cluster 2 profile

C. IDHwt vs mt

Sample with cluster 6 dominant Astrocytoma grade III, IDHmt

D

E. Cluster 6 profile

F. IDHwt vs mt

Figure 3

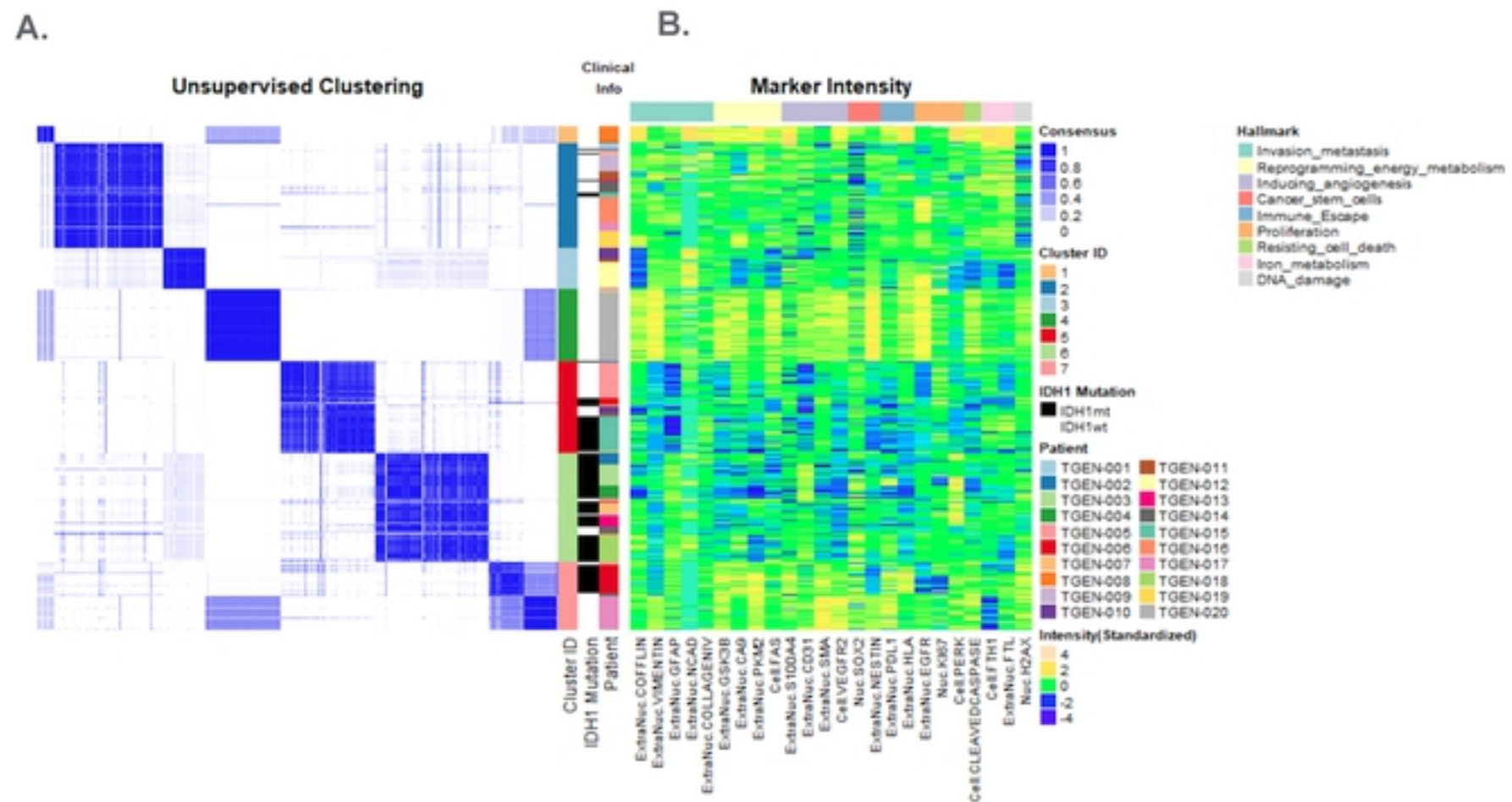# Figure 2: Distribution and clustering of cells based on protein expression in treatment naïve glioma patients

Figure 2

Figure 5: Correlation between IDH1 mutation status and cell phenotype at both gene and protein level.
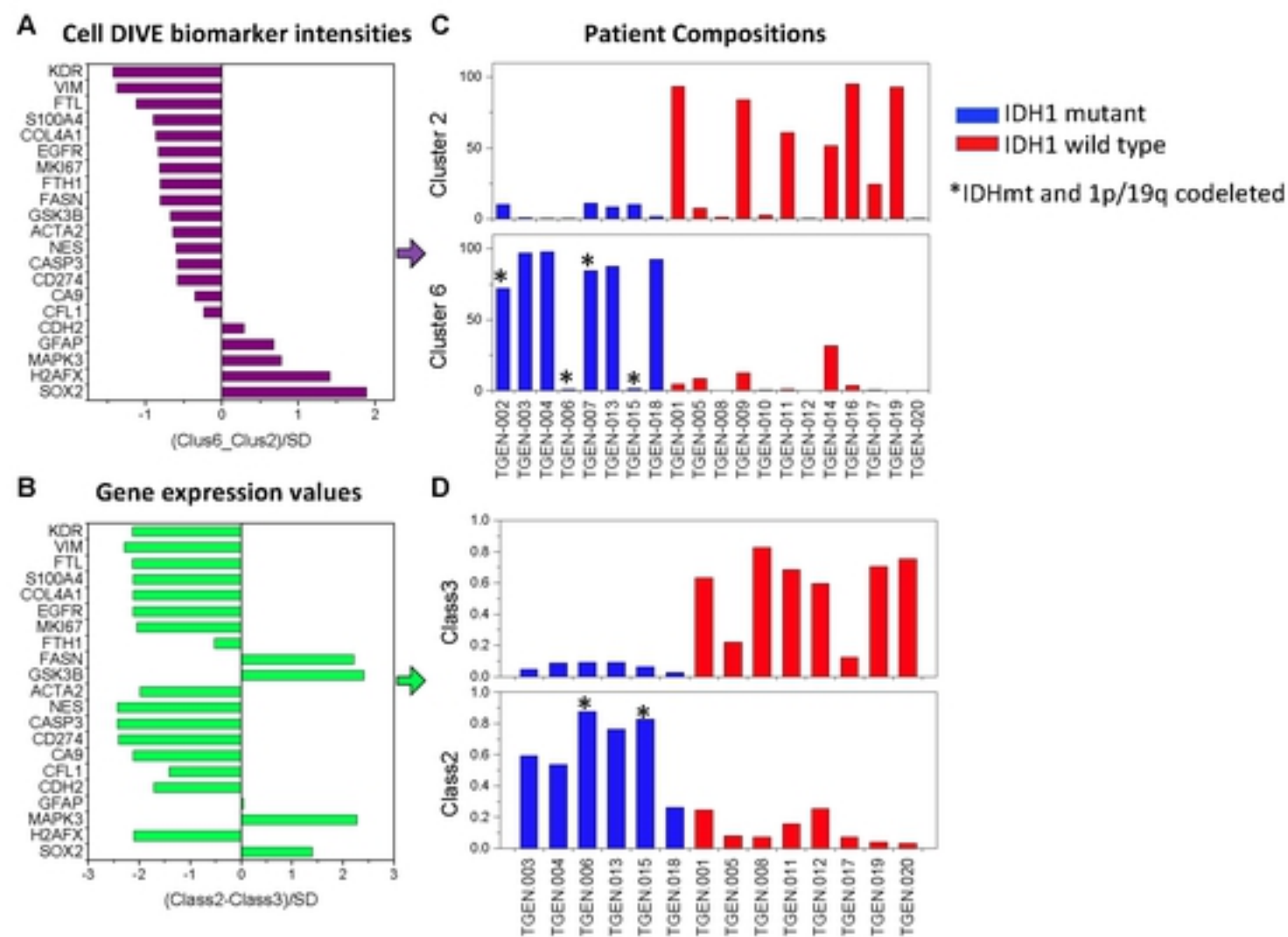
Figure 5

Figure 8: Multiscale modality integration including IDH1 mutation, clinical data, MRI, RNA and protein expression for the angiogenesis markers and corresponding cell clusters.
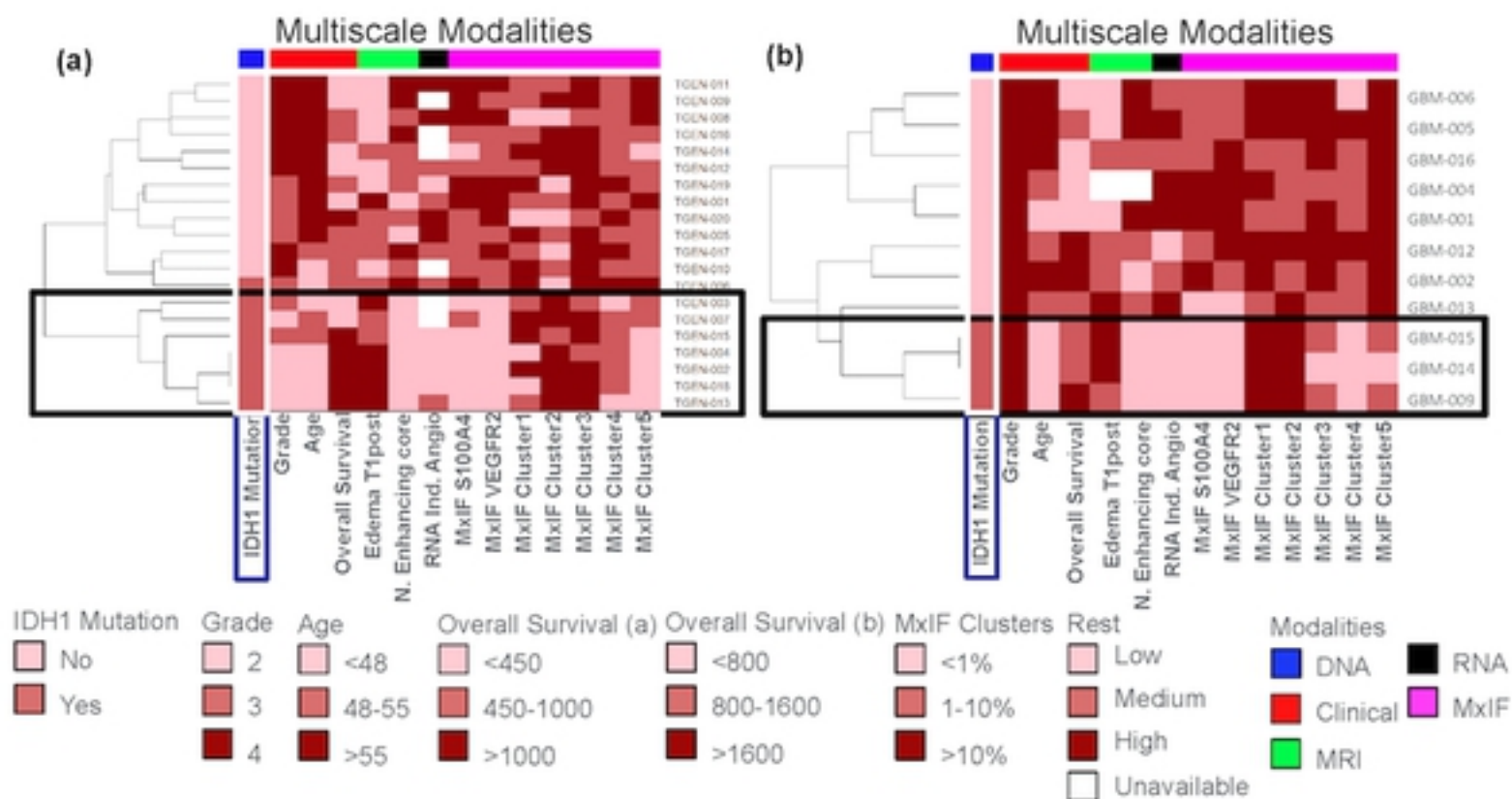
Figure 8

Figure 4: Cell cluster composition and oncoprint of treatment naive gliomas
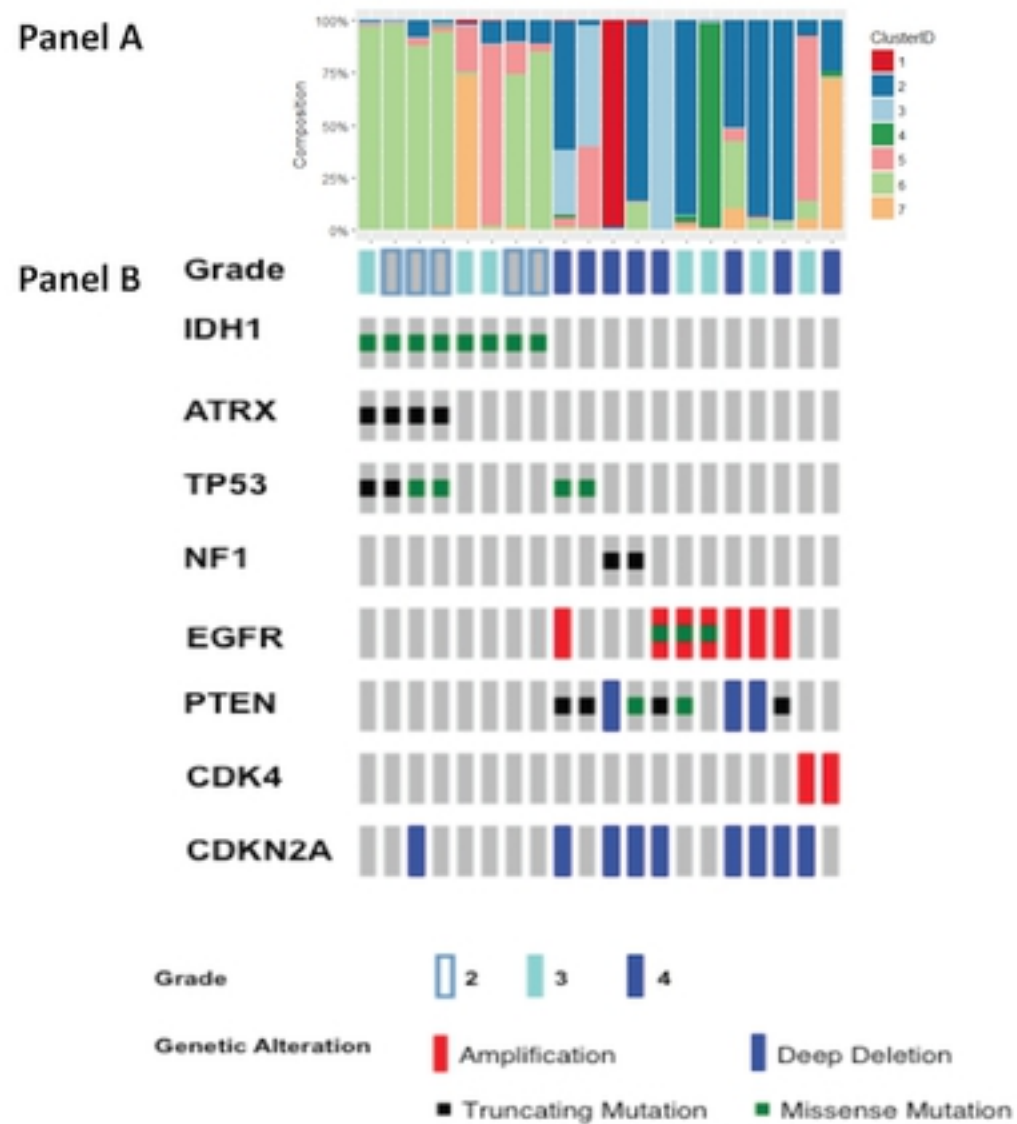
Figure 4